Journal of Aerosol Science 180 (2024) 106392

Contents lists available at ScienceDirect

Journal of Aerosol Science

journal homepage: www.elsevier.com/locate/jaerosci

Differences and similarities in optical properties of coated fractal soot and its surrogates

Egor V. Demidov [a], Ogochukwu Y. Enekwizu [b,1], Ali Hasani [a,2], Chong Qiu [c], Alexei F. Khalizov [a,b,*]

[a] Department of Chemistry and Environmental Science, New Jersey Institute of Technology, Newark, 07102, NJ, United States
[b] Department of Chemical and Materials Engineering, New Jersey Institute of Technology, Newark, 07102, NJ, United States
[c] Chemical Engineering Department, University of New Haven, West Haven, 06516, CT, United States

ARTICLE INFO

Editor: Dr. Chris Hogan

Keywords:
Aerosol
Soot
Black carbon
Carbon black
Nigrosin
Aerosol aging
Light absorption
Light scattering

ABSTRACT

Atmospheric soot (or black carbon, BC) affects climate through solar light absorption and scattering, which depend strongly on the particle morphology and composition. Initially, soot particles are fractal aggregates of spherules made of elemental carbon (EC), but condensation of atmospheric trace vapors adds non-EC materials and often results in particle compaction. The optical properties of such processed soot differ from those of fractal soot, and the changes are caused both by particle volume increase from coating addition and by restructuring of the EC backbone. In laboratory studies of soot optics, surrogates such as carbon black (CB) and nigrosin are often used in place of flame-generated soot. Our goal was to investigate if compositional and morphological differences between these surrogates and soot may produce different processing rates and optical responses. In our experiments, we generated fractal soot, compact CB, agglomerated CB (via coagulation of compact CB), and spherical nigrosin aerosol particles, subjected them to supersaturated vapor of dioctyl sebacate (DOS) to form a coating layer, and investigated the morphological response of these four particle types to coating addition and removal. Using coated and coated-denuded aerosol particles with known composition and morphology, we quantified the contributions of volume increase and restructuring to light scattering and absorption enhancements. By comparing experimental measurements against different particle optics models we show that it is crucial to account for larger, multiply charged particles present in the mobility-classified aerosol. Producing a disproportionately high contribution to absolute values of optical cross sections, such larger particles also result in lesser optical enhancements due to slower growth by vapor condensation. Scattering increases for all particle types due to the addition of a coating layer, and also due to restructuring for fractal soot (strongly) and agglomerated CB (weakly). Absorption increases only due to coating addition caused by the coating layer for all particle types. We find that simple optical models, such as Mie, are often sufficient to provide reasonable closure with experimental results for bare and coated aerosols, but only after accounting for the contributions from multiply charged particles, both in terms of their stronger optical cross sections and slower condensational growth. We conclude that CB is an appropriate surrogate for soot in aerosol aging studies where the effects of restructuring do not need to be considered and that nigrosin

* Corresponding author at: Department of Chemistry and Environmental Science, New Jersey Institute of Technology, Newark, 07102, NJ, United States.
E-mail address: khalizov@njit.edu (A.F. Khalizov).
[1] Now at: Brookhaven National Laboratory, Upton, 11973, New York, United States.
[2] Now at: Division of Applied Mechanics, US Food and Drug Administration, Silver Spring, 10903, Maryland, United States.

https://doi.org/10.1016/j.jaerosci.2024.106392
Received 4 March 2024; Received in revised form 26 April 2024; Accepted 13 May 2024
Available online 23 May 2024

can be used as a general model for light-absorbing aerosols but is not representative of optical properties of soot.

Nomenclature

m	fg	Mass of a particle
D	nm	Electrical mobility diameter of a particle
D_{ve}	nm	Volume-equivalent diameter of a particle
ρ	g/cm^3	Material mass density
V	cm^3	Volume
b	1/Mm	Optical coefficient
C	μm^2	Optical cross section
N	1/cm^3	Aerosol number density
N_s	1	Number of primary particles in a fractal aggregate
k_0	1	Fractal pre-exponential factor
D_f	1	Fractal dimension
R_s	nm	Radius of gyration
d_p	nm	Diameter of a primary particle in a fractal aggregate
Δr_{ve}	nm	Volume-equivalent coating thickness
Δr_m	nm	Coating thickness of a primary particle
GF_d	1	Electrical mobility diameter growth factor
GF_m	1	Mass growth factor
f_i	1	Relative contribution of mode i to the optical cross section, number fraction

1. Introduction

Atmospheric aerosols affect climate indirectly by changing cloud properties (Lohmann & Feichter, 2005; Tao, Chen, Li, Wang, & Zhang, 2012) and directly by scattering and absorbing sunlight (Chylek & Wong, 1995). Among many types of aerosols, soot (or black carbon) is of particular interest, as it strongly absorbs light, thus contributing to global warming, as much as one-third of the contribution of CO_2 (Haywood & Boucher, 2000). Moreover, in many locations worldwide, including major megacities, direct solar heating caused by soot aerosols is comparable with the heating due to greenhouse gases (Ramanathan & Carmichael, 2008). Soot particles suspended in the atmosphere are subject to continuous aging, which changes their microphysical and optical properties, and thus their climatic impacts. Condensation is one of the major aging mechanisms of soot (Saathoff et al., 2003), and it has been extensively studied using experimental and modeling approaches, including the effects of negative surface curvature (Chen et al., 2018; Ivanova, Khalizov, & Gor, 2020) and carbon structure (Ivanova, Emelianova, Khalizov, & Gor, 2022) on the localization of condensate.

Soot particles are fractal aggregates of graphitic primary spherules and their principal source is the incomplete combustion of carbonaceous matter. Combustion can be used to generate soot aerosols in the laboratory to study their transformations and properties. However, since particle size, organic carbon content, morphology, and concentration of flame-generated soot are highly sensitive to combustion and sampling conditions (Slowik et al., 2007, 2004), researchers often prefer to use pre-made products instead, like carbon black (CB). Such products are manufactured industrially to serve as ink pigments, material additives, etc., making them inexpensive and readily available (Long, Nascarella, & Valberg, 2013). In spite of a different name, carbon black is inherently the same material as soot. The combustion conditions for CB are well controlled leading to less variability in the generated products. The key difference between CB and flame-generated soot is that the former can be distributed in the form of an aqueous suspension, where aggregates are present as near-spherical particles. In contrast, soot generated and sampled in a flame retains its fractal morphology until the controlled aging process is deliberately initiated, allowing to evaluate changes in optical properties that are induced by not only a coating layer addition, but also by restructuring of the particles.

Advantages of using CB in place of soot include high carbon content, stable number density and size distribution, constant morphology and composition, ease of generation, and safety, as generation does not involve flames. Indeed, a simple atomizer that nebulizes a suspension of carbon black particles can generate a stable output over extended time. “Cab-O-Jet” (a brand CB) has been used in a number of studies, including an intercomparison of aerosol absorption cross sections measured with photoacoustic spectroscopy (Zangmeister & Radney, 2018), the size and wavelength dependence of optical properties of bare particles (Zangmeister, Grimes, Dickerson, & Radney, 2019), and also a comparison of mass absorption spectra obtained at different labs against other surrogates, such as graphene nanoplatelets and fullerene soot (Zangmeister et al., 2018). These studies concluded that measurements reported by different labs were generally consistent and that surrogates are suitable for instrumental intercomparison. That would likely not be the case with the flame-generated soot, because slight variations in combustion conditions can lead to drastic differences in particle morphology and composition (Moore et al., 2014), and hence optics. Another brand of CB, “Regal Black” (Sedlacek, Lewis, Onasch, Lambe, & Davidovits, 2015), was used as proxy for collapsed soot to study the response of a Single-Particle Soot

Photometer (SP2) to morphology of composite particles produced by coagulation of light absorbing and non-absorbing aerosols, including sodium chloride, ammonium sulfate, and dioctyl sebacate.

Some researchers go as far as to use nigrosin as a surrogate for absorbing aerosols (Brem, Mena Gonzalez, Meyers, Bond, & Rood, 2012; Dial, Hiemstra, & Thompson, 2010; Drinovec et al., 2022; Kondo et al., 2009; Sedlacek & Lee, 2007; Veghte, Moore, Jensen, & Freedman, 2015). Nigrosin is a water-soluble organic dye for negative staining of bacteria, which can be nebulized from its solution, and when droplets evaporate upon mixing with dry air, spherical particles are formed. Since nigrosin particles are not fractal, they lack the ability to restructure. Also, being solid spheres, nigrosin particles lack interstitial space that can be present in CB and compacted soot. One factor making nigrosin an attractive surrogate is that extinction and scattering cross sections can be easily calculated for its spherical particles, presumably making experimental results easy to verify computationally. However, when particles are size classified based on their electrical mobility, the resulting aerosol is not truly monodisperse, containing a fraction of multiply charged particles of larger sizes (McMurry, Wang, Park, & Ehara, 2002; Pagels, Khalizov, McMurry, & Zhang, 2009). These larger particles have significantly higher absorption and scattering cross-sections, which can bias high optical measurements (Moosmuller, Chakrabarty, & Arnott, 2009) and cause a significant deviation from theoretical predictions. There are ways to account for the presence of multiply-charged particles for both bare and coated aerosols (Bueno et al., 2011; Forestieri et al., 2018), but the procedures are not always trivial and additional measurements are often required.

This study explores experimentally how flame-generated soot aggregates and their surrogates (commercial CB and nigrosin) respond morphologically and optically to coating by a low-volatility organic compound, dioctyl sebacate (DOS). For CB, we report measurements for both compact aggregates and agglomerates of compact aggregates. Corrections for multiple charging are applied and their efficacy is analyzed and discussed for different particle types. Finally, the optical properties of soot, two forms of CB, and nigrosin are compared against each other and also against three commonly used optical models, to determine applicability ranges for the optical models and soot surrogates.

2. Methodology

The system used to generate and process aerosols is illustrated in Fig. 1. It comprised an aerosol generation unit (either an atomizer or an inverted diffusion flame burner), a differential mobility analyzer (DMA, TSI Model 3081A) with home-built recirculating sheath flow and high voltage control to produce electrical mobility-classified aerosol, a temperature-controlled coating chamber, a thermal denuder to remove coating from aerosol (Orsini, Wiedensohler, Stratmann, & Covert, 1999), an aerosol particle mass analyzer (APM, Kanomax Model 3601) to measure mass of aerosol particles, a second DMA to measure electrical mobility diameter of aerosol particles processed by coating or coating followed by denuding, a cavity attenuated phase shift spectrometer (CAPS PM_{SSA}, Aerodyne Research, 525 nm wavelength) to measure aerosol extinction and scattering coefficients, and a condensation particle counter (CPC, TSI Model 3772) to measure aerosol particle number density. The components of the system were connected with stainless steel tubing joined together end-to-end with short segments of conductive silicone tubing. The entire system was controlled by LabView codes, and a detailed description of the system and its individual components can be found in our previous work (Chen et al., 2016; Fan, Dawson, Chen, Qiu, & Khalizov, 2018).

2.1. Particle generation and processing

Soot was generated by incomplete combustion of natural gas in an inverted diffusion flame burner (Coderre, Thomson, Snelling, & Johnson, 2011; Stipe, Higgins, Lucas, Koshland, & Sawyer, 2005) and sampled using an ejector dilutor. Carbon black suspension (Cab-O-Jet 200, Cabot Corporation) and nigrosin solution (Nigrosin water soluble, Alfa Aesar) were prepared with distilled water and corresponding aerosols were generated with a constant output atomizer (TSI Model 3076). To generate compact CB, the nebulized aqueous aerosol was immediately diluted with dry air. To generate agglomerated CB, the nebulized aerosol was diluted a few centimeters downstream from the atomizer, which provided sufficient residence time for concentrated aerosol droplets to coagulate, producing agglomerated CB particles after drying. In some experiments, polystyrene latex (PSL) aerosols of different particle sizes were generated from suspensions of nanospheres (3000 Series Nanosphere, Thermo Scientific). The aerosols were brought to equilibrium charge distribution with a bipolar ^{210}Po charger (Staticmaster Static Eliminator, 500 μCi) and size-classified with DMA1. It is important to note that particles carrying multiple charges behave as if they were smaller in an electric field of the DMA. Therefore, aerosol after DMA1 is pseudo-monodisperse.

The size-classified aerosol was coated by passing it through a temperature-controlled coating chamber, which is a cylindrical borosilicate glass container (45 cm length and 2 cm inner diameter) partially filled with dioctyl sebacate (DOS) and wrapped in heating tape and insulation. DOS was selected as the coating material because of its low volatility (saturated vapor pressure of 9.69×10^{-6} Pa at 25 °C) and frequent use to study soot processing and optics. Adjusting the temperature of the coating chamber allowed the control of DOS condensation on particles. After every temperature adjustment, we waited for the particle mass to reach a steady-state value. In some experiments, the condensed coating material was subsequently removed from particles by passing them through a thermal denuder operated at 300 °C. All bare particles were passed through the denuder prior to processing to ensure that any optical response of coated-denuded particles was not induced by the high temperature in the denuder. Particle mass and electrical mobility diameter of processed aerosol were measured by sending the flow through the APM and DMA2, respectively. Both DMAs were operated at a sheath-to-sample flow ratio of 6.5, using sample and sheath flows of 1.0 and 6.5 liters per minute (lpm). The APM operated at a sample flow of 0.3 lpm, which was achieved by removing 0.7 lpm before the APM and then adding

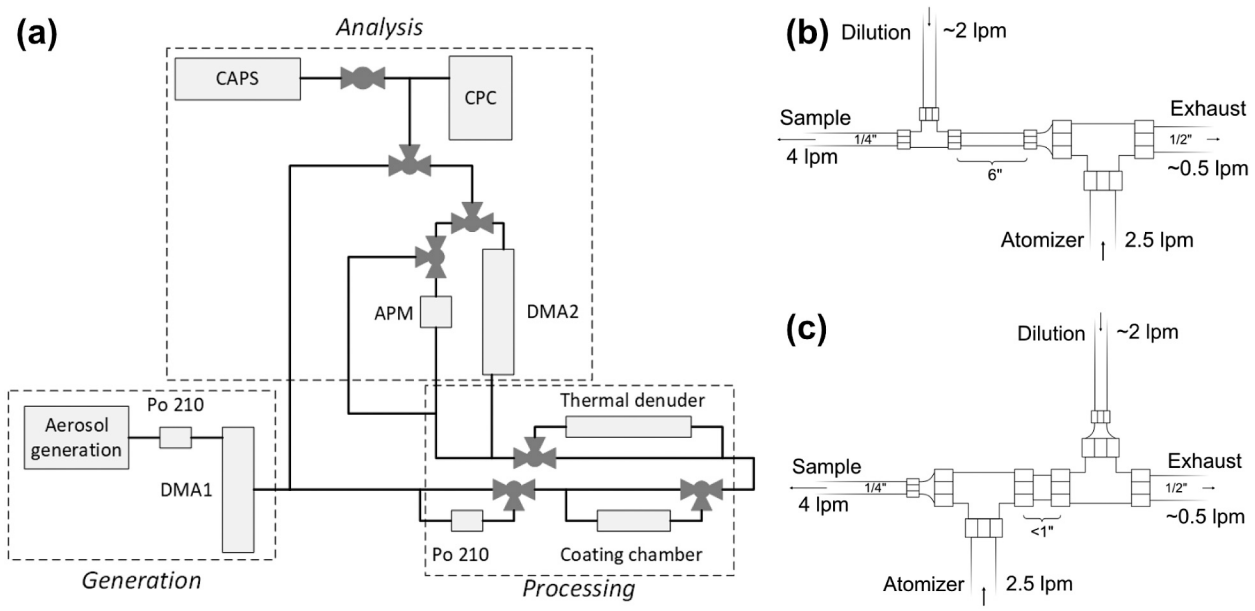

Fig. 1. (a) Aerosol generation and processing system, (b) dilution configuration used to generate agglomerated CB, and (c) dilution configuration used to generate compact CB.

0.7 lpm of filtered clean air after the APM, using volumetric flow controllers connected to a vacuum pump and pressurized air, respectively.

Mass measurements were used to determine the amount of coating condensed and electrical mobility diameter was used to quantify the extent of restructuring. For a single particle size selected by DMA1, an APM scan obtains a mass distribution and mean mass is determined by fitting the distribution to a Gaussian-like function. Mass of processed particles, m was normalized by mass of fresh particles m_0 to obtain the mass growth factor.

$$GF_m = \frac{m}{m_0} \tag{1}$$

Mass growth factor was converted into volume equivalent coating thickness, Δr_{ve}, to facilitate the comparison in the amount of coating gained by particles of different initial volume-equivalent diameters (Khalizov et al., 2013).

$$\Delta r_{ve} = \frac{1}{2} D_{ve,0} \left(\sqrt[3]{\frac{V}{V_0}} - 1 \right) = \frac{1}{2} D_{ve,0} \left(\sqrt[3]{1 + \frac{\rho_{\text{core}}}{\rho_{\text{shell}}} \left(GF_m - 1 \right)} - 1 \right) \tag{2}$$

In the equation, $D_{\text{ve},0}$ is volume-equivalent diameter of bare particles, V is volume of a coated particle, V_0 is volume of a bare particle, ρ_{core} is material density of a bare particle, and ρ_{shell} is density of the coating material.

Similarly, the electrical mobility diameter of processed particles, D was normalized by the electrical mobility diameter of fresh particles, D_0, to obtain the electrical mobility diameter growth factor.

$$GF_d = \frac{D}{D_0} \tag{3}$$

GF_d was obtained from Tandem DMA (TDMA) scans, where particles were size-classified with DMA1, processed by coating or coating-denuding, and then their size distribution was measured with DMA2.

2.2. Particle sample collection and imaging

Samples of size-classified unprocessed aerosol particles were collected on silicon chips, using a custom-built electrostatic precipitator (Chen, Enekwizu, Ma, Zakharov, & Khalizov, 2017; Dixkens & Fissan, 1999) placed after DMA1. In the precipitator, high voltage (3–4 kV) applied to the chip holder created an electric field between the chip and grounded body of the precipitator, causing charged aerosol particles to travel toward and deposit on the silicon chip. After an hour of collection, chips were removed from the precipitator and imaged with a scanning electron microscope (SEM, JEOL JSM-7900F). Before collection, silicon chips were prepared by washing with methanol in an ultrasound bath and drying with nitrogen gas. To quantify particle compactness, convexity was calculated from SEM images as the ratio of the particle projected area (A_p) to the area of a convex hull polygon.

$$\text{Convexity} = \frac{A_p}{A_{polygon}} \tag{4}$$

2.3. Optical measurements

To measure number density and optical properties of aerosol concurrently, a makeup flow of 0.87 lpm was added and then the sample flow was split in two separate flows directed to CAPS PM_{SSA} (0.87 lpm) and CPC (1.0 lpm), respectively. The splitting was done isokinetically with a tee, where the outlets were on a straight line perpendicular to the inlet. The splitting point was placed 1 m downstream from the dilution point, where the solenoid valve of the make up flow controller served as an orifice to create turbulence and promote mixing. The distances from the split to CAPS PM_{SSA} and CPC were adjusted to ensure equal wall losses, so that the particle number density measured by the CPC corresponded to the number density within the CAPS PM_{SSA} cell. We found that it was crucial to install a denuder filled with XB-17 (a mixture of activated charcoal and permanganate-impregnated alumina, General Carbon Corp.) after DMA1 during experiments with flame-generated soot to remove traces of NO_2 produced by the burner. NO_2 is a strong light absorber at 525 nm and its concentration is highly sensitive to combustion conditions. In the absence of the denuder, light extinction measurements were subject to significant variability, requiring that baselines to be taken frequently.

The CAPS PM_{SSA} measured extinction and scattering coefficients (b) of bare and processed aerosol. Extinction and scattering coefficients of particles were determined by subtracting the baseline coefficients of particle-free gas from the measured coefficients of the aerosol. Absorption coefficients were calculated as a difference of extinction and scattering coefficients (Khalizov, Xue, Wang, Zheng, & Zhang, 2009; Moosmuller et al., 2009).

$$b_{\text{abs}} = b_{\text{ext}} - b_{\text{sca}} \tag{5}$$

The coefficients were converted to cross sections (C) by normalizing them by aerosol number density (N):

$$C = \frac{b}{N} \tag{6}$$

To obtain accurate optical data, scattering and extinction coefficients were recorded every five seconds over three minutes for each measurement. Arithmetic mean of the cross sections acquired over a three-minute interval was calculated and reported as the optical measurement. Baselines were taken prior to each measurement, where aerosol flow was redirected through a filter (United Filtration DIF-BN60) located inside the CAPS PM_{SSA} to flush its optics cell and measure extinction and scattering of gas without particles.

2.4. Numerical aggregate generation for discrete dipole approximation calculations

Soot aggregates of fractal ($D_f < 2.1$) and compact ($D_f > 2.1$) morphologies were simulated using a cluster–cluster aggregation (CCA) algorithm developed by Mackowski (1995). The CCA algorithm, described here in brief, is based on a hierarchical scheme of aggregation of smaller sub-clusters, which obey the fractal scaling law (Jullien, 1987),

$$N_s = k_0 \left(\frac{2R_s}{d_p} \right)^{D_f} \tag{7}$$

where N_s is the number of primary particles, k_0 is the pre-exponential factor, R_s is the radius of gyration, d_p is the diameter of primary units, and D_f is the fractal dimension. In this context, where all the primary particles are assumed to be of the same size, R_g is defined as the root mean squared distance of primary particles from the center of mass of the aggregate. Equal-sized primary particles are characteristic of many laboratory generated soot aggregates (Enekwizu, Singh, & Khalizov, 2020; Wentzel, Gorzawski, Naumann, Saathoff, & Weinbruch, 2003).

Aggregate generation involves sequentially combining smaller sub-aggregates into bigger clusters until the target aggregate size is reached. Every time two sub-aggregates are combined into a cluster, radius of gyration of the formed cluster, $R_{g,\text{new}}$, depends on radii of gyration of its two constituent sub-aggregates, $R_{g,1}$ and $R_{g,2}$, and on how those sub-aggregates are combined. Therefore, $R_{g,\text{new}}$ of the formed cluster can be controlled by varying the orientations of the sub-aggregates and the location of the point where they are joined. A function $R_{g,\text{new}}(R_{g,1}, R_{g,2}, D_f, k_0)$ is derived from the fractal scaling law and the definition of R_g. Then, at every step where sub-aggregates are combined, $R_{g,\text{new}}$ is prescribed by the fractal scaling law and orientations and joining positions are varied randomly until $R_{g,\text{new}}$ of the combined cluster is within uncertainty tolerance from the target value. Thus, by constraining the way sub-aggregates are combined, an aggregate conforming to Eq. (7) is generated. Aggregates produced by the CCA algorithm are representative of real soot particles formed via diffusion-limited cluster aggregation (Filippov, Zurita, & Rosner, 2000).

To discretize the aggregate for use with DDA, a three-dimensional Cartesian grid is created and the generated fractal aggregate is placed in this Cartesian space. For each spherical particle comprising the aggregate, grid elements that fall within the boundary of the sphere are filled with black carbon. To add a uniform coating to the discretized aggregate, the function described in Enekwizu et al. (2020) is used to compute the boundary of the coating layer and all the grid elements that are within the boundary of the coating, but are not already filled with black carbon, are then filled with the coating material.

2.5. Optical models

Mie theory, Rayleigh–Debye–Gans (RDG), and discrete dipole approximation (DDA) were used to predict optical properties of bare and coated particles. Mie theory provides a solution for electromagnetic wave scattering and extinction by a sphere (Bohren & Huffman, 1983). A modification of Mie for coated spheres, implemented by Liu, Wang, Yu, Xu, and Shen (2007), was used to model coated particles in this study. Mie provides an exact solution for spherical particles (*e.g.*, nigrosin) and should be in a

Table 1
Refractive indices of materials used in optical calculations.

Material	Complex refractive index at 530 nm
Soot/carbon black[a]	$1.73 + 0.60i$
Nigrosin[b]	$1.71 + 0.27i$
Liquid organic compounds[c]	$1.43 + 0.00i$

[a] Chang and Charalampopoulos (1990).
[b] Lang-Yona et al. (2009).
[c] Enekwizu et al. (2020).

reasonable agreement with experimental data for compact particles, such CB, thickly coated soot, or coated-denuded soot, due to their near-spherical shape.

The RDG approximation (Kerker & Loebl, 1969; Sorensen, 2001) can be used to provide a better estimate of optical properties in the case of fractal aggregates. Absorption cross section (Eq. (8)) of an aggregate is approximated by a product of the absorption cross section of an individual primary particle ($C_{\mathrm{abs,monomer}}$) and the number of individual primary particles (N_s). In conjunction with core–shell Mie theory, RDG can be used to predict light absorption by thinly coated fractal aggregates (RDG-Mie). We do not consider RDG scattering because it requires the fractal dimension of aggregates, experimental determination of which is beyond the scope of this study. To extend the RDG approach to coated aggregates, the coating material is distributed over the primary particles as spherical shells and absorption cross sections are computed for the coated primary particles using core–shell Mie. Then, absorption cross sections of coated primary particles are scaled to aggregates according to RDG theory.

$$C_{\mathrm{abs,aggregate}} = N C_{\mathrm{abs,monomer}} \tag{8}$$

When the diameter of primary particles in an aggregate is known, volume equivalent coating thickness of a primary particle can be related to volume equivalent coating thickness of the aggregate with Eq. (9):

$$\Delta r_m = d_m \frac{\Delta r_{ve}}{D_0} \tag{9}$$

DDA (Draine & Flatau, 1994) is a versatile approach for predicting the optical properties of particles of arbitrary geometry that has been used in a large number of soot modeling studies (Dong, Zhao, & Liu, 2015; Kahnert, Nousiainen, & Lindqvist, 2013; Yon, Bescond, & Liu, 2015). In DDA, the particle shape is described as a collection of small discrete volumes (dipoles) that interact with electromagnetic waves and each other. To converge to an accurate solution, the interdipole separation, d, has to be chosen sufficiently small such that the quantity $|n|kd < 1$, where n is the complex refractive index and $k = 2\pi/\lambda$ is the scattering wave vector, with λ being the incident wavelength. This is to ensure that the dipole approximation holds (Yurkin & Kahnert, 2013) and that the geometry of the particle is well approximated by an array of dipoles (Liu, Teng, Zhu, Yurkin, & Yung, 2018).

Optical modeling was performed using the refractive indices shown in Table 1. The refractive index of soot is based on the expression reported by Chang and Charalampopoulos (1990). For a wavelength of 530 nm, the refractive index was $1.73 + 0.6i$, falling within the range recommended by Bond and Bergstrom (2006) for visible light. The refractive index of the organic coating was assumed to be $1.43 + 0i$ and is representative of many organic materials (Haynes, 2014), including DOS, which was used in our experiments. By comparing DOS with other chemicals of similar structure, we found that the refractive index varied by less than ± 0.03, causing a $\pm 3.5\%$ variation in scattering and $\pm 2.5\%$ variation in absorption by a 150 nm absorbing sphere with a 20 nm coating. Such variation is within the uncertainty range of our experimental measurements, as discussed later in Section 3.2.1. The refractive index of nigrosin varies among literature sources due to differences in chemical composition of nigrosin used by different groups. We investigated a range of indices from different sources (Bluvshtein, Flores, Riziq, & Rudich, 2012; Dinar et al., 2008; Flores et al., 2014; Lack, Lovejoy, Baynard, Pettersson, & Ravishankara, 2006; Lang-Yona, Rudich, Segre, Dinar, & Abo-Riziq, 2009). Using nigrosin refractive indexes from different sources resulted in a standard deviation of 10% for calculated absorption cross sections and 12% for calculated scattering cross sections of bare nigrosin particles.

Optical measurements were conducted at 525 nm wavelength, while DDA calculations were performed for 530 nm wavelength. According to our sensitivity analysis, the difference in scattering is 0.4% and the difference in absorption is 0.3% for a 150 nm absorbing sphere with a 20 nm coating at 525 nm and 530 nm wavelength. This difference is within the uncertainty of our experimental measurements, which means that DDA calculations are representative of experimental data.

For this study, the Amsterdam DDA (ADDA) version 1.3 (Yurkin & Hoekstra, 2020), an open-source C implementation of DDA, was used. For each bare or coated soot aggregate, orientation-averaged extinction, scattering, and absorption cross-sections (C_{ext}, C_{sca}, C_{abs}) were determined. The interdipole separation, d was varied from 2 nm down to 0.8 nm, resulting in approximately 1 400 to 22 000 dipoles per single monomer volume. The maximum dipole size of 2 nm was only used for thickly coated aggregates (*i.e.*, $\Delta r_{ve} \geq 18$ nm). Small dipole sizes ensured that both the coating and morphological features were accurately represented *i.e.*, there were no shape approximation errors. Under these circumstances $|n|kd$, was less than 0.1 and satisfied the restriction set by Kahnert, Nousiainen, Lindqvist, and Ebert (2012) for obtaining accurate optical predictions for soot aggregates. The calculated optical properties presented in this study are an average of three aggregate realizations belonging to the same class of fractal parameters (N_s, R_s, D_f, k_0). The relative standard deviations (RSD) obtained were less than 1%.

3. Results and discussion

3.1. Particle size and morphology

3.1.1. Bare particles of different types

Particle samples of each of the four aerosol types used in this study were collected and imaged by SEM. Samples were collected from size-classified aerosol at the same mobility diameters, as used for optical measurements: 240 nm for soot and agglomerated CB, 150 nm for nigrosin and compact CB. Soot aggregates (Fig. 2a) are highly fractal whereas nigrosin particles are fully spherical (Fig. 2b). Morphology of the atomized CB strongly depends on the aerosol dilution approach. The two types of dilution configuration used in this study are illustrated in Fig. 1. If droplets produced upon atomization are immediately diluted with dry air, CB aggregates are compact and nearly spherical (Fig. 2d). However, if the generated aqueous aerosol is not diluted immediately (Fig. 1b), droplets coalesce and, after drying, produce semi-fractal aggregates made of multiple compact units (Fig. 2c). Adjusting aerosol residence time before dilution with dry air (Fig. 1c) can be used to vary the morphology of CB from fully compact particles to agglomerates of compact particles. An important feature observed in most images, and especially prominent in the image of nigrosin, is the presence of larger multiply charged particles. For instance, for nigrosin, in addition to the most numerous singly charged 147 nm particles (as measured from the SEM image shown in Fig. 2b), we observed the presence of fewer numbers of larger doubly charged (235 nm) and even triply charged (294 nm) particles. Additionally, nigrosin shows the presence of doublets among the 147 nm particles, which were formed by coalescense of dry particles.

Particle morphology can be described quantitatively using different metrics, such as convexity and mass-mobility scaling exponent (China et al., 2015). Average convexities of particles in Fig. 2 were found to be (a) 0.61 ± 0.01, (b) 0.96 ± 0.01, (c) 0.78 ± 0.01, and (d) 0.90 ± 0.01, high values for more compact particles in agreement with visual observations.

The mass-mobility exponent can be determined from the dependence of the particle mass on the electrical mobility diameter (Eq. (10)), where for spherical particles, mass is proportional to the cube of diameter. This relationship can be written in relative form, where the electrical mobility diameter is normalized by a reference electrical mobility diameter, and mass is normalized by mass of particles of that reference electrical mobility diameter, allowing us to eliminate the proportionality constant (Eq. (11)).

$$m \propto D^3 \tag{10}$$

$$\frac{m}{m_{\mathrm{ref}}} = \left(\frac{D}{D_{\mathrm{ref}}}\right)^{\epsilon} \tag{11}$$

Particle deviation from a spherical geometry causes the exponent in Eq. (11) to deviate from 3, while the overall power law dependence remains valid. Hence, we can define a general mass-mobility law, where ϵ is mass-mobility exponent, which is similar, but not equivalent to D_f.

To determine compactness, mass of particles of different electrical mobility diameters can be measured and ϵ can be calculated by fitting the data to Eq. (11). Such mass-mobility measurements were performed for the four aerosol types mentioned above and also for PSL, using 150 nm–350 nm electrical mobility diameter particles (Fig. 3). Perfectly spherical PSL particles produced mass mobility exponent of 3.00 ± 0.01. Nigrosin particles, albeit spherical, produced somewhat lower ϵ approaching 2.95 ± 0.01. Soot aggregates were highly fractal, with a mass-mobility exponent of 2.36 ± 0.01. Carbon black particles fell between highly fractal soot and spherical nigrosin, with the mass-mobility exponent for compact CB closer to nigrosin (2.88 ± 0.01) and that of agglomerated CB closer to soot (2.68 ± 0.01).

Mass-mobility measurements support the trend in convexities determined from SEM images and provide an alternative quantitative way to compare the morphology of different particle types. It is interesting to note that ϵ for nigrosin is 2.95 and not exactly 3.00, as measured for PSL. This deviation from the mass-mobility exponent of 3.00, as expected for spherical particles, can be due to a slight decrease in particle effective density with increasing mobility diameter. Particle effective density is defined as the ratio of particle mass to its mobility diameter based volume. The mass distributions of nigrosin particles in Fig. S2 exhibit a tail towards lower masses as the mobility diameter increases, confirming this observation.

3.1.2. Particles processed by vapor condensation

In coating experiments, mobility-classified particles of different types were exposed to supersaturated DOS vapor and then changes in the mobility diameter and mass were measured. The initial mobility diameters of the particles were chosen such that their initial volume equivalent diameters (D_{ve}) were approximately equal between the different types of aerosols used,

$$D_{ve} = \sqrt[3]{\frac{6m}{\pi\rho}} \tag{12}$$

where m is particle mass and ρ is material mass density. Electrical mobility and volume equivalent diameters, as well as particle masses and material mass densities, are provided in Table 2.

Fractal and compact particles responded differently to coating, as shown in Fig. 4a, where the dependence of electrical mobility diameter growth factor (GF_d) on mass growth factor (GF_m) is plotted for coated aerosols. With the addition of DOS, GF_d increased rapidly for nigrosin, but gradually for compact CB. For agglomerated CB, the value of GF_d remained nearly unchanged (less than 1% change), increasing only slightly for $GF_m > 2$. In the case of soot, GF_d decreased notably (14% decrease) for lower coating mass, but began to increase for $GF_m > 2.2$.

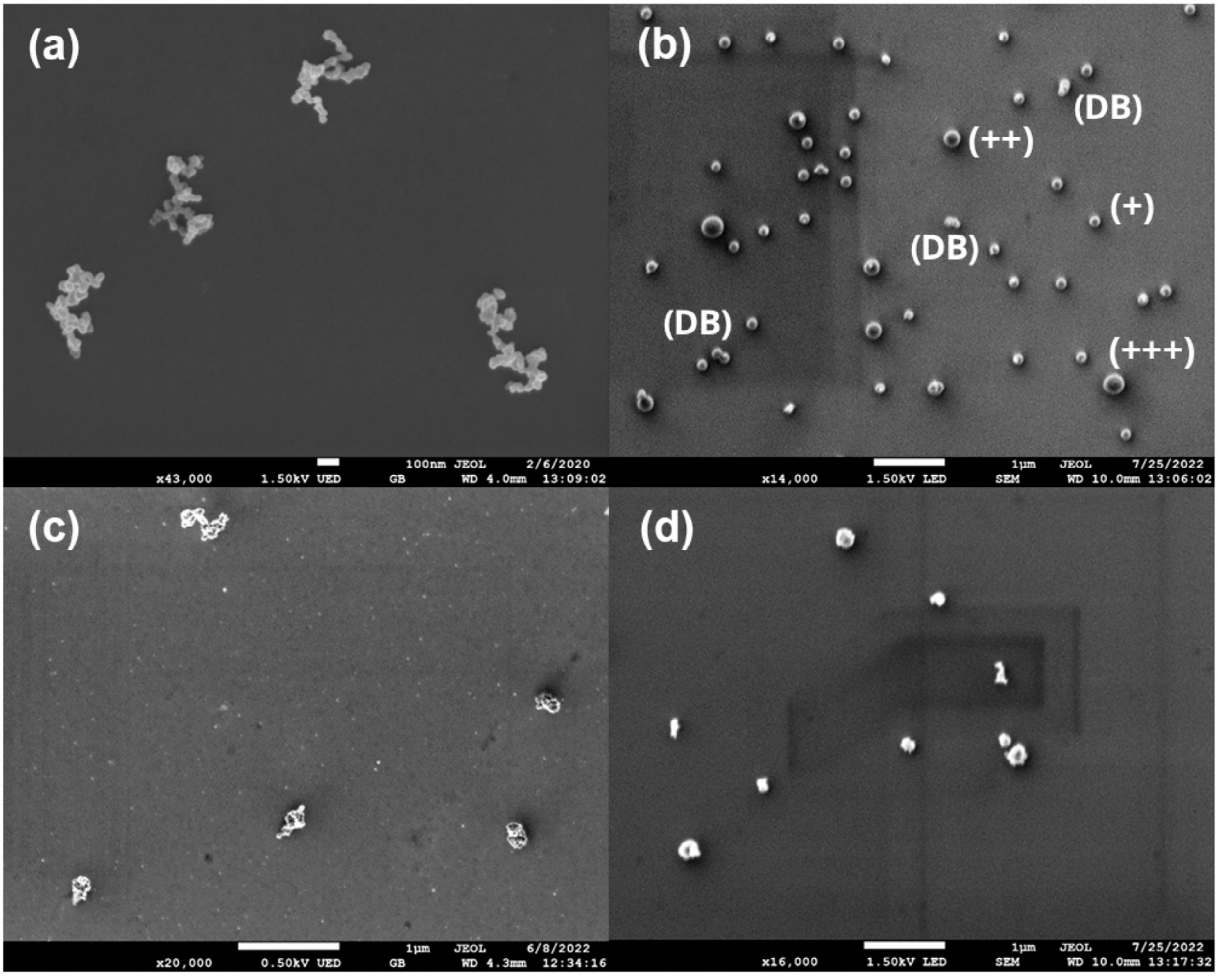

Fig. 2. SEM images of: (a) flame-generated soot, (b) nigrosin, (c) agglomerated CB, and (d) compact CB. In the image for nigrosin, (+), (++), and (+++) mark the singly, double, and triply charged particles with diameters of 147, 235, and 294 nm, respectively, and (DB) marks doublets from coagulation. Mobility diameters used to classify these particles: (a) 240 nm, (b) 150 nm, (c) 240 nm, and (d) 150 nm.

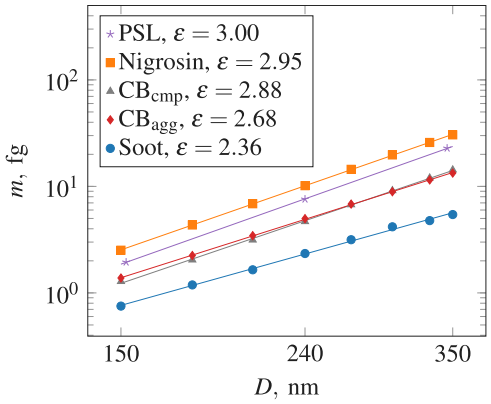

Fig. 3. Dependence of mass on the electrical mobility diameter for bare particles of different types. Listed mass mobility exponents (ε) are obtained from exponential fits. Data used to generate this figure is available in Fig. S1.

Compact CB particles grew less in mobility diameter than nigrosin particles for the same GF_m because they are made of multiple smaller primary particles and contain significant void space, with an estimated void fraction of 60%, above the minimum void

Table 2
Electrical mobility and volume-equivalent diameters of bare aerosol particles, along with particle mass and material mass density.

	D_m, nm	m, fg	ρ, g/cm^3	D_{ve}, nm
Soot	240	2.367	1.77[a]	137
Nigrosin	150	2.488	1.41[b]	150
CB (compact)	150	1.283	1.77[c]	111
CB (agglomerated)	240	4.571	1.77[c]	170

[a] Park, Kittelson, Zachariah, and McMurry (2004).
[b] Measured in this study (see mass-mobility measurements).
[c] Assuming that ρ of CB is the same as soot.

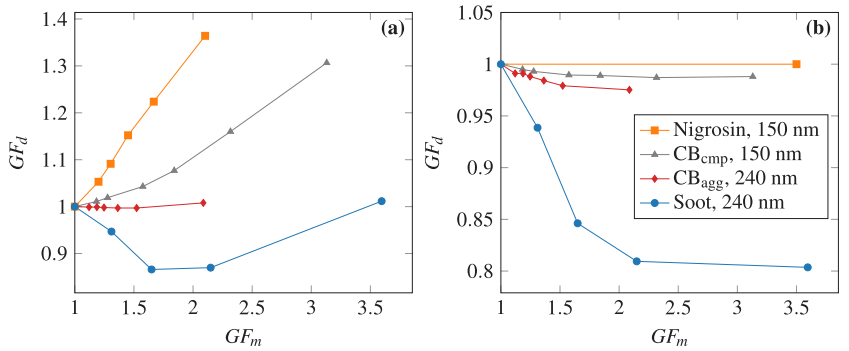

Fig. 4. Electrical mobility diameter growth factor (GF_d) vs. mass growth factor (GF_m) upon processing of different types of particles: (a) DOS coated particles and (b) DOS-coated-denuded particles. Volume equivalent diameters of bare particles are 150 nm for nigrosin, 137 nm for soot, 111 nm for compact CB, and 170 nm for agglomerated CB.

fraction of 36% in fully compacted aggregates obtained considering a random distribution of primary particles in the globules formed by restructuring (Mikhailov, Vlasenko, Podgorny, Ramanathan, & Corrigan, 2006), an indication that CB aggregates remained irregular and not fully compacted, as shown in Fig. 4b. Part of the DOS coating occupied the voids inside the compact CB particles instead of forming a layer around them, thus resulting in less size growth than for solid nigrosin spheres for the same relative increase in mass.

Unlike compact particles, fractal soot and aggregated CB restructure upon condensation of DOS, with higher coating mass leading to greater compaction, as reflected by a decrease in GF_d. Since particle compaction is partially offset by the addition of the coating, the latter must be removed by thermal denuding to discriminate the contributions from restructuring and coating volume addition. As shown in Fig. 4b, the GF_d of coated-denuded soot drops substantially, reaching maximum compaction at $GF_m \approx 2$, as similarly reported in Chen et al. (2020). By maximum compaction we refer to the minimum GF_d that a soot aggregate can reach during restructuring upon exposure to the DOS coating. Only then the soot particle mobility diameter begins to increase during subsequent coating addition (Fig. 4a). In contrast to fractal soot, agglomerated CB particles undergo minimal restructuring, while for compact CB particles restructuring is barely noticeable. The negligible restructuring of compact CB is unsurprising because particles were generated from an aqueous suspension where aggregates underwent complete restructuring during manufacturing and upon droplet evaporation during nebulization (Ma, Zangmeister, Gigault, Mulholland, & Zachariah, 2013). The somewhat more pronounced restructuring of agglomerated CB was due to partial folding of the branches (Fig. 2c), each branch made of a compact CB particle (Fig. 2d). These drastically different responses in volume equivalent coating thickness and morphology between particles of the four types produce different optical responses, as described in Section 3.2.

3.1.3. Growth by vapor condensation of multiply charged particles

Multiply charged particles are larger and acquire coatings at a lower rate than the singly-charged smaller particles because in continuum regime the rate of vapor condensation is inversely proportional to particle radius (Seinfeld & Pandis, 2016), when the amount of coating is expressed in terms of coating thickness. This effect of slower coating thickness growth is less pronounced for fractal aggregates, at least while they remain lightly coated, because both singly charged smaller aggregates and multiply charged larger aggregates are composed of primary spherules of approximately the same diameter, which is smaller than the gas mean free path. Hence, individual primary spherules in both aggregates gain condensate under molecular condensation regime at the same rate. Experimentally, the slower rate of coating thickness growth of non-fractal multiply charged particles can be observed by adding a second diffusion charger after DMA1 during TDMA scans, allowing the discrimination between particles of different charges in the pseudo-monodisperse aerosol, as shown in Fig. 5 for fresh and coated nigrosin aerosol. Coating thicknesses calculated from mobility diameters of smaller and larger particles before and after coating application obtained from those scans (Table 3) indicate that the larger particles acquired a 24% thinner coating layer.

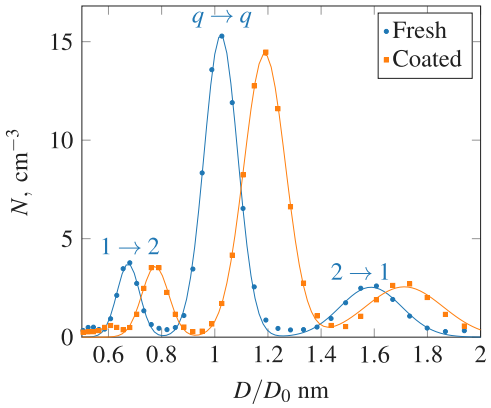

Fig. 5. Recharged TDMA scans of fresh and coated 150 nm nigrosin. X-axis, the electrical mobility diameter, is normalized by D_0 = 150 nm. $q \to q$ indicates particles that were singly charged prior to recharging and remained singly charged after, but this mode still contains a significant number of doubly charged particles (Khalizov et al., 2009), $2 \to 1$ indicates particles that were doubly charged prior to recharging and became singly charged after, $1 \to 2$ indicates particles that were singly charged prior to recharging and became doubly charged after. While there are also triply charged particles in the size-classified aerosol, they are not visible in this TDMA scan due to limitations on the scan range with the sample flow rate used during optical measurements. Broader scans of bare particles that show triply charged particles are available in Fig. S5.

Table 3
Coating thickness of singly and doubly charged nigrosin particles of 150 nm initial mobility diameter.
Source: Data from Fig. 5.

	$1 \to 2$	$q \to q$	$2 \to 1$
$GF_{d,\text{bare}}$	0.673	1.020	1.587
$GF_{d,\text{coated}}$	0.773	1.187	1.713
D_{bare}, nm	154	153	238
D_{coated}, nm	178	178	257
Δr_{ve}, nm	12.0	12.5	9.5

3.2. Optical measurements

3.2.1. Measurement uncertainty

Prior to discussing the optical results, we need to understand the uncertainties associated with each type of measurement. We measure the change in optical properties of aerosols in response to coating and compare experimental results with calculations. Our results and conclusions depend on optical, mass, and size measurements and their respective uncertainties. Also, since the experiments described in this study take hours, variability in bare aerosol throughout the day can introduce additional uncertainty. In this section, we discuss uncertainty contributions from various factors and what was done to minimize them.

A methodological uncertainty is introduced by a limitation of CAPS PM_{SSA}: it underestimates scattering of particles that exhibit a significant fraction of forward and backward scattering. In the Mie scattering regime, scattering anisotropy increases with particle size. Particles under 250 nm in diameter do not exhibit a large amount of forward and backward scattering, thus making the truncation error of CAPS PM_{SSA} negligible. This effect sets an upper bound on the size of particles used in experiments. On the other hand, according to the manufacturer, the standard deviations in scattering and extinction coefficients for particle-free sample are 0.1 Mm^{-1} and 0.03 Mm^{-1} for 3 min averaging time. Using PSL spheres of 240 nm diameter, we found that the deviation between scattering and extinction coefficients measured by CAPS PM_{SSA} and predicted using Mie were 2.0 Mm^{-1} and 1.5 Mm^{-1} respectively. The magnitude of optical coefficients of particles increases with particle size. Hence, a larger particle size is preferable to maximize the magnitude of measured optical coefficients relative to the reported resolution and precision. Based on these considerations, we restricted our optical measurements to particles between 150 nm and 240 nm mobility diameter, which should minimize the methodological uncertainty. Statistical uncertainties are discussed further.

To verify the reproducibility of measurements made over several days, optical measurements of 150 nm bare nigrosin were performed on three different days. Absorption cross sections varied by <1% from day to day and scattering cross sections had a standard deviation of <3%. Consistency of nigrosin measurements over several days indicates that any significant variance observed in fresh soot optical measurements is related to variations in particle morphology and slight changes in chemistry, caused by changing combustion conditions. To quantify the variance of soot morphology throughout one experiment and to reduce its impact on the uncertainty of enhancements, a fresh soot optical measurement was taken after each processed soot measurement. Then, to calculate optical enhancements, optical cross sections of processed particles were normalized by the optical cross sections of the temporally closest fresh soot measurement. Both the variance of fresh soot optics throughout an experiment and the variance between experiments were quantified. The relative standard deviations of scattering and absorption cross sections of bare soot within

one experiment were normally within 5%. The relative standard deviations of scattering and absorption cross sections of bare soot over 16 different experiments were 26% and 21% respectively. Thus, due to variations in morphology, the optical response of soot shows some variation from day to day, but remains stable within one day.

To verify the accuracy of size classification, the DMA was calibrated using a suspension of PSL containing 150 nm, 240 nm, and 350 nm nominal diameter spheres. The actual sphere sizes reported by the PSL manufacturer were 152 ± 5 nm, 240 ± 5 nm, 345 ± 7 nm. To quantify the uncertainty in particle mass measurements, the same PSL suspension as the one used for DMA verification with PSL particles of three nominal sizes was nebulized. The DMA was used to size-select particles of a nominal diameter (152 nm, 240 nm, or 345 nm) and the APM was used to measure their mass. Measured masses were compared to the masses expected for spheres of the respective diameter with density of 1.055 g/cm^3. The measured masses were within <1% deviation from the expected values.

3.2.2. The effect of multiple charging on measured optical cross sections of bare particles

We begin our discussion with analysis of absolute optical cross sections, which often are subject to significant uncertainty. A major source of this uncertainty stems from size classification of particles based on their electrical mobility, which may introduce a significant fraction of particles carrying multiple charges in a nominally monodisperse aerosol. As described in the previous section, such particles are larger than the particles of interest and hence absorb and scatter light stronger, resulting in an overestimation of these optical properties. The contribution from these multiply charged particles must be accounted for when deriving absolute absorption and scattering cross sections, optical enhancements, and single-scattering albedo (SSA), as described below.

Most commonly, the size-classified aerosol is passed through a second diffusion charger, which re-charges the particles and allows to reveal the nearly-true distribution of multiply-charged particles among the size-selected particles on a TDMA scan. Alternatively, one can use electron microscopy images of particle samples to estimate fractions of larger multiply charged particles, at least for non-fractal particles of regular shapes. When the aerosol number density is low, the contribution from some particle modes, such as from triply charged particles is difficult to quantify accurately, but their contribution to measured scattering and absorption cross sections can still be significant. Below we illustrate the application of both approaches, recharging-TDMA and SEM imaging, towards elucidating the fraction of multiply charged particles in a nominally monodisperse sample of spherical nigrosin particles, and evaluating the contribution of such particles to absorption and scattering cross sections.

Based on the recharged TDMA scan of the 150 nm mobility diameter nigrosin shown in Fig. S5b and using equations S6–S8, number fractions (f_i) of singly, doubly, and triply charged particles were found to be 76%, 19%, and 5%, respectively. The sizes of these particles were 150 nm, 236 nm, and 315 nm, corresponding to the peaks at 1.02, 1.59, and 2.11 in the TDMA scan (Fig. S5b). Counting particles of three different sizes in the SEM image (Fig. 2b) provided similar albeit not identical fractions, 84%, 11%, and 4%. The difference between the two methods is a result of several effects, including insufficient statistics due to the small number of examined particles in the SEM image and the non-negligible "contamination" of the 1 → 1 particle mode in Fig. S5b by doubly charged particles (Khalizov et al., 2009). Unlike this "contamination", the statistics can be improved by increasing the number of interrogated particles, and hence in the following example we use the fractions obtained from the SEM image to calculate the contributions to absorption and scattering cross sections from each individual particle mode, along with the total cross sections comprising the sum of all three modes,

$$C_{\mathrm{abs/sca,tot}} = \sum_i f_i C_{\mathrm{abs/sca},i} \tag{13}$$

where f_i is the number fraction of the respective mode, $C_{\mathrm{abs/sca},i}$ is the absorption or scattering cross section of the respective mode, and $C_{\mathrm{abs/sca,tot}}$ is the overall scattering or absorption cross section of the aerosol. The relative contribution of mode i to total cross section is

$$f_{\mathrm{abs/sca}} = \frac{C_{\mathrm{abs/sca},i} \times f_i}{C_{\mathrm{abs/sca,tot}}} \tag{14}$$

As shown in Table 4, triply charged nigrosin particles, being only 4% by number, contributed to 22% of the total absorption cross section and 34% of the total scattering cross section. The total estimated absorption cross section including all three modes is 1.78×10^{-14} m^2, while the absorption cross section consisting only of 150 nm particles is 1.04×10^{-14} m^2. Thus, presence of doubly and triply charged particles in a mobility-classified aerosol leads to overestimation of the absorption cross section by 71%. The bias due to larger particle modes is even more significant for scattering, where the total estimated scattering cross section is 1.36×10^{-14} m^2, while the scattering cross section of the 150 nm particle mode is 5.06×10^{-15} m^2, indicating a 169% overestimation. For comparison, experimentally measured absorption and scattering cross sections for 150 nm nigrosin measured without recharging were 2.00×10^{-14} m^2 and 1.87×10^{-14} m^2 respectively. Thus, factoring the optical contributions of multiply charged particles into calculated optical properties reduced the bias, but still failed to provide full agreement for a number of reasons, *e.g.*, the singly-charged particle mode in Fig. S5b still containing a fraction of doubly charged particles (Khalizov et al., 2009), the presence of particles with higher order charges that could not be detected due to their large size and small number density, *etc.*

One can physically reduce the fraction of multiply charged particles in a mobility-classified aerosol by selecting particles with diameters that are on the falling edge (or towards the tail end) of the incoming aerosol size distribution (Fig. S1). As shown in Fig. S5, whereas 150 nm electrical mobility classified aerosols of different types contain large fractions of doubly charged particles, the fraction of those particles is significantly lower in the 240 nm aerosols. Hence, a simple way to minimize the contribution of multiply charged particles during experimental measurements is by carefully selecting the target particle size during mobility classification. In the following section, we explore how the presence of multiply charged particles affects the relative optical enhancements when bare particles become coated.

Table 4
Absorption and scattering characteristics of nigrosin particles at 525 nm wavelength calculated with Mie. Quantitative statistics are based on particle counts from the SEM image shown in Fig. 2b.

	150 nm	236 nm	315 nm
Number fraction (f_i)	0.84	0.11	0.04
Particle mass, fg	2.49	9.70	23.08
Absorption			
C_{abs}, $m^2 \times 10^{14}$	1.04	4.70	9.64
$C_{abs} \times f_i$, $m^2 \times 10^{14}$	0.876	0.517	0.386
Contribution, $\frac{C_{abs} \times f}{C_{abs,total}}$	0.493	0.291	0.217
$C_{abs,tot}$, $m^2 \times 10^{14}$	1.78 (total of three modes)		
Scattering			
C_{sca}, $m^2 \times 10^{14}$	0.506	4.32	11.6
$C_{sca} \times f_i$, $m^2 \times 10^{14}$	0.425	0.475	0.464
Contribution, $\frac{C_{sca} \times f_i}{C_{sca,tot}}$	0.312	0.348	0.340
$C_{sca,tot}$, $m^2 \times 10^{14}$	1.36 (total of three modes)		

3.2.3. Optical response of coated particles

Fig. 6 shows experimentally measured enhancements in light absorption and scattering for the different particle types subjected to processing via coating by DOS (a, c, e) or coating combined with thermal denuding (b, d, f), along with the corresponding changes in SSA. The enhancements were obtained by normalizing experimentally measured optical cross sections of processed aerosols by optical cross sections of bare aerosols. The SSA was calculated as a ratio of scattering and extinction cross sections for the same aerosol, either fresh or processed. Presenting data in a normalized form facilitates comparison of different particle types, which have significantly different absolute values of absorption and scattering cross sections (see Fig. S7). Also, such representation is common for optical data reporting in laboratory, field, and computational studies (Enekwizu et al., 2020; Fierce et al., 2020; Khalizov et al., 2009).

The addition of coating enhances light absorption for all particle types (Fig. 6a), with the largest enhancement ($E_{abs} = 1.30$) observed for spherical nigrosin particles and the lowest ($E_{abs} = 1.15$) for fractal soot particles, for a 30 nm thick coating (volume equivalent coating thickness, as defined by Eq. (2)). For soot, the magnitude of enhancement is in agreement with previous experimental measurements (Cross et al., 2010; Khalizov et al., 2009). The enhancement in light scattering is more substantial than for absorption (Fig. 6c), with the largest values observed for fractal soot ($E_{sca} = 3.5$ at 30 nm coating thickness), followed by the other particle types ($E_{sca} \approx 2$). During coating, absorption and scattering can be altered by changes in both the particle mixing state (addition of a coating layer) and morphology (restructuring), with the exception of nigrosin, where only the mixing state is altered. Water-soluble nigrosin that was used in our experiments does not dissolve in DOS, as verified by an experiment. By removing the coating layer via thermal denuding, it is possible to isolate changes induced by the restructured particle morphology from the changes due to coating addition.

Thermal denuding of coated particles reduces the enhancement in absorption to 1.00 ± 0.05 for all particle types (Fig. 6). Thus, absorption is largely independent of the soot particle morphology at 525 nm wavelength (Radney et al., 2014) but can be significantly increased by coating addition, where the transparent coating layer intensifies light absorption by the particle core. Scattering enhancement also decreases after denuding, approaching unity for all particle types except for soot ($E_{sca} = 1.45$ at 30 nm volume equivalent coating thickness), as shown in Fig. 6d. The significant residual scattering enhancement in soot is the result of restructuring experienced by fractal particles. As shown previously (Sorensen, 2001), the primary particles in fractal aggregates scatter light poorly due to their small size relative to the light wavelength, but restructuring reduces the aggregate radius of gyration, bringing the primary particles to a closer configuration that increases constructive wave interference and leads to a significant increase in scattering (Khalizov et al., 2009). The more fractal the particle is initially, the higher the increase in scattering will be after processing. The joint effect of restructuring and coating addition is responsible for fractal soot having the largest scattering enhancement during coating.

For bare particles, SSA is the lowest for fractal soot and the highest for nigrosin (Fig. 6e). With the addition of the coating shell, SSA increases with approximately the same slope for all particle types, although fractal soot shows a faster rate of increase in the 15–30 nm region, where it undergoes significant restructuring. This region can be clearly seen in experiments with coated-denuded soot (Fig. 6f). For other particle types, SSA of bare and coated-denuded particles remain unchanged within experimental uncertainty.

3.2.4. Comparison of experiments with simple optics models

Figs. 7 and 8 compare experimentally measured absorption and scattering enhancements for all particle types against calculations by the commonly used core–shell Mie optical model, which predicts optical properties exactly for spherical particles and often produces a reasonable agreement for compact aggregates. In the case of soot and CB, we also included the calculation by the RDG-Mie approach.

When comparing experiments against Mie calculations and taking into account the measurement uncertainty, the agreement in absorption enhancement is better for nigrosin, agglomerated CB, and compact CB (Fig. 7b–d) than for soot and compact CB (Fig. 7a), especially at volume equivalent coating thicknesses below 25 nm. The RDG-Mie values agree with measured absorption enhancement for soot with volume equivalent coating thicknesses below 30 nm, but become lower than experimental values for

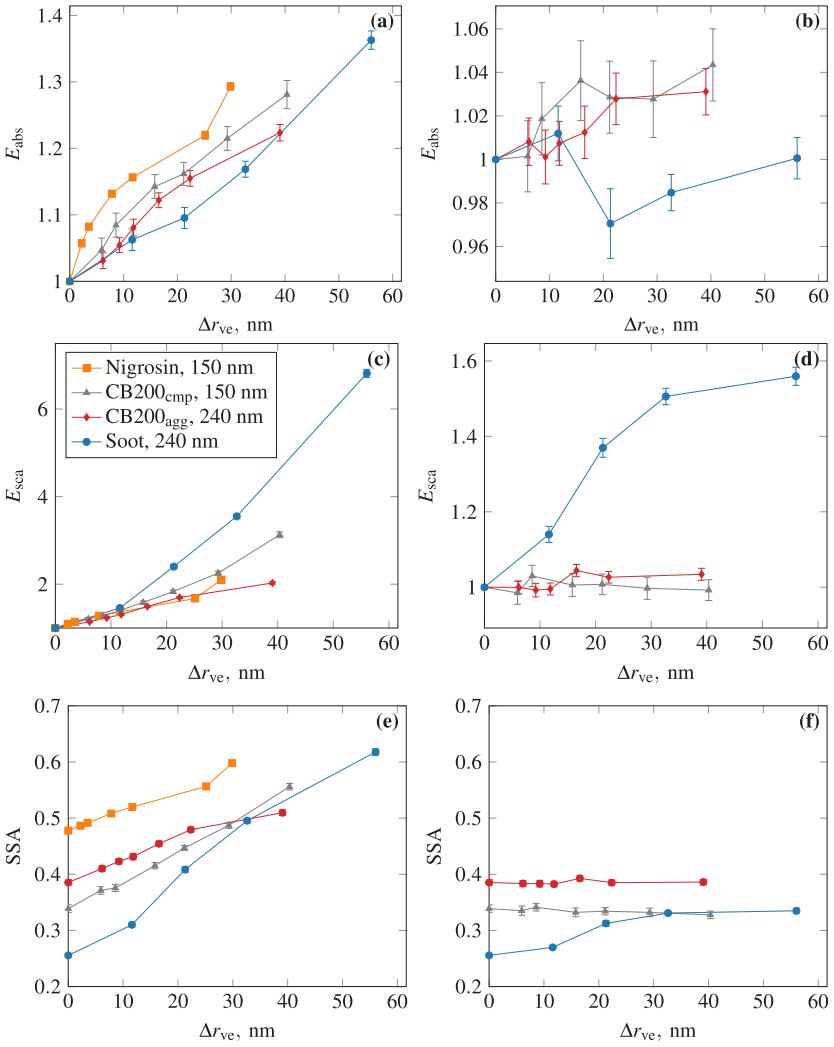

Fig. 6. Experimentally measured enhancement in light absorption (a, b), scattering (c, d), and SSA (e, f) for coated (a, c, e) and coated-denuded (b, d, f) aerosols of different types. Relative uncertainty for optical enhancements ranges from 5% (for bare particles with weak scattering signal) to 1% (for thickly coated particles with strong scattering and extinction). Volume equivalent diameters of bare particles are 150 nm for nigrosin, 137 nm for soot, 111 nm for compact CB, and 170 nm for agglomerated CB.

thicker coatings. Such a trend can be readily explained by the fact that, for absorption, the RDG approach assumes no optical interaction between primary particles. This assumption is approximately valid for fractal aggregates, but not for compact aggregates. For this reason, RDG-Mie performed poorly in predicting absorption enhancement for both types of CB particles. For scattering enhancement predicted by Mie, there was a reasonable agreement with experimental measurements for soot and agglomerated CB, (Fig. 8a,d; solid lines), but for nigrosin and compact CB the deviation was high and the curves diverged progressively with increasing coating thickness. SSA was significantly underestimated by Mie calculations for all aerosol types (Fig. 9), with the lowest deviation in the case of fractal soot.

Many factors can contribute to differences in experimental optical measurements for soot and its surrogates and also to disagreement between the experimental optical measurements and optical model predictions. These factors include differences in particle morphology between soot and its surrogates, the presence of multiply charged larger particles in nominally size-classified aerosol, and an implicit assumption that singly and larger multiply-charged particles acquire coatings at the same rate (Fierce, Bond, Bauer, Mena, & Riemer, 2016). In the following, we assess and discuss contributions from some of these factors.

3.2.5. The effect of multiple charging on coated particle optics

It is well recognized that the larger, multiply charged particles bias absolute optical cross sections high (Forestieri et al., 2018; Khalizov et al., 2009). We found that presenting optical changes as enhancements expressed relative to unprocessed aerosol does not cancel out the contribution of multiply charged particles, as shown in Figs. 7 and 8, which compare experimental measurements

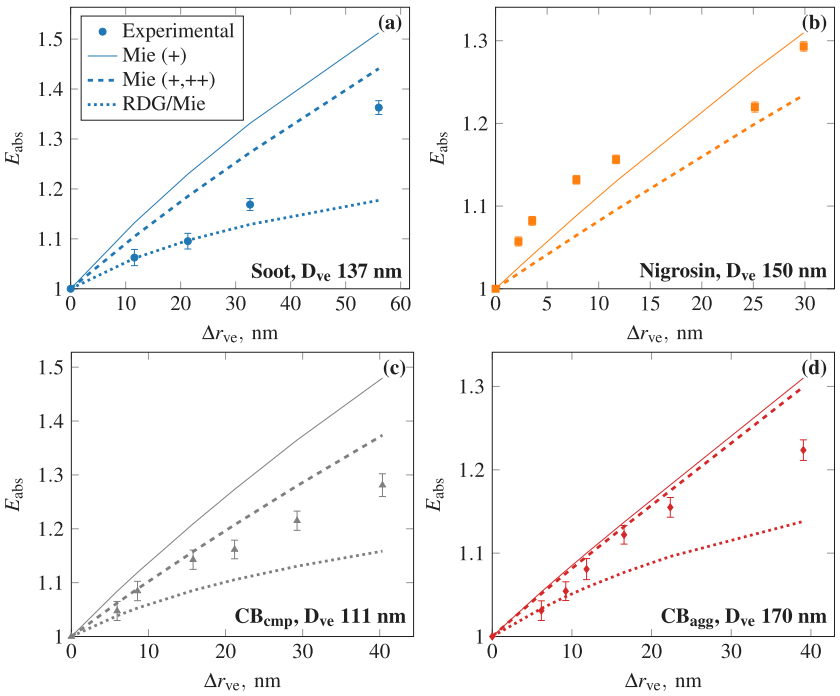

Fig. 7. Measured and calculated absorption enhancements for compact soot (a), nigrosin (b), compact CB (c), and agglomerated CB (d). Measured data are presented by markers, calculated with Mie theory by solid line, and calculated with Mie by accounting for doubly charged particles by dashed line. For cases (a) and (d), the dashed and solid line overlap due to a negligible fraction of double charged particles. Volume equivalent and mobility diameters for all aerosol types are available in Table 2.

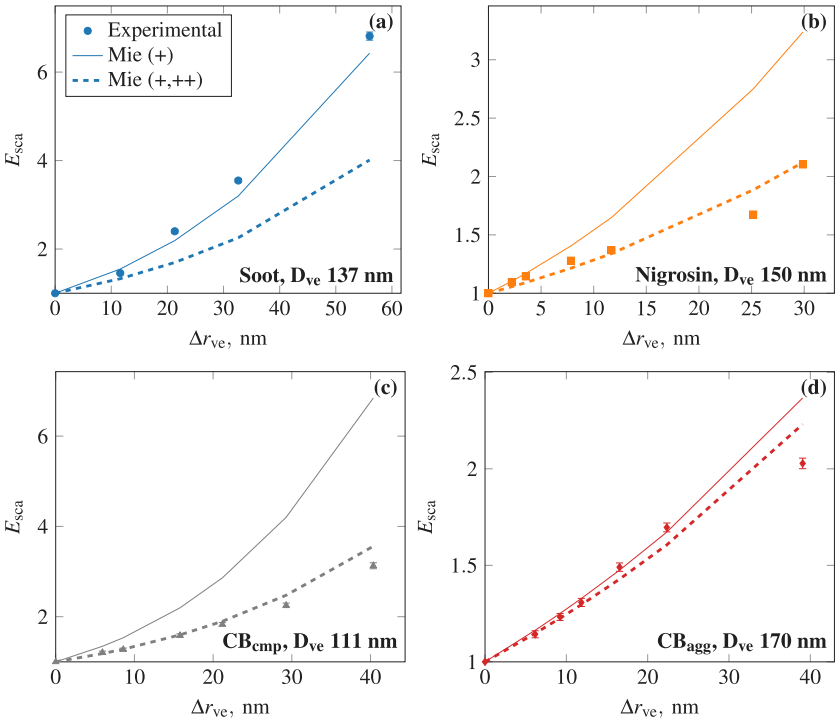

Fig. 8. Measured and calculated scattering enhancements for compact soot (a), nigrosin (b), compact CB (c), and agglomerated CB (d). Measured data are shown by markers, calculated with Mie theory by solid line, and calculated with Mie by accounting for doubly charged particles by dashed line. For cases (a) and (d), the dashed and solid line overlap due to a negligible fraction of double charged particles. Volume equivalent and mobility diameters for all aerosol types are available in Table 2.

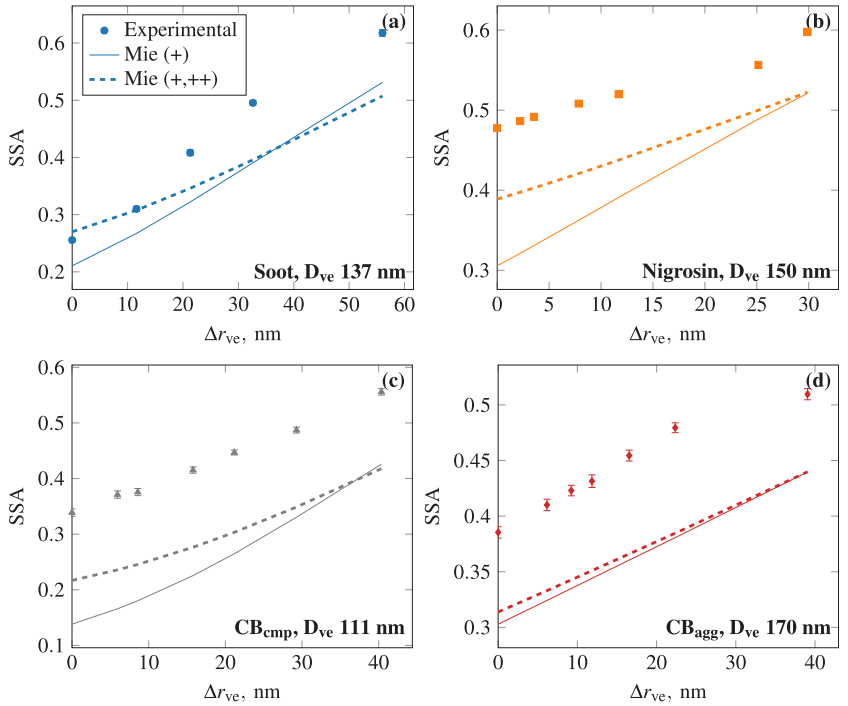

Fig. 9. Measured and calculated SSA for compact soot (a), nigrosin (b), compact CB (c), and agglomerated CB (d). Measured data are shown by markers, calculated with core–shell Mie theory by solid line, and calculated with Mie by accounting for doubly charged particles by dashed line. For cases (a) and (d), the dashed and solid line overlap due to a negligible fraction of double charged particles. Volume equivalent and mobility diameters for all aerosol types are available in Table 2.

against Mie theory predictions made under an assumption of a monodisperse aerosol. Notably, for relative enhancements the calculations overestimate the experimental data, in sharp contrast with the absolute cross sections, where the calculations underestimate the experimental data.

The lower experimental enhancements are caused by the multiply charged particles being coated at a lower rate, but absorbing and scattering light stronger than the singly-charged particles, which are the particles of interest. The size-dependent rate of volume equivalent coating thickness growth leads to a non-uniform population mixing state of the aerosol (Fierce et al., 2016), which is made of thickly-coated singly charged particles and thinly-coated multiply charged particles. Due to their lower volume equivalent coating thicknesses coupled with large contributions to absolute light absorption and scattering, multiply charged particles produce lower optical enhancements, biasing overall experimental enhancements low. A similar effect has been observed in a field study (Cappa et al., 2012), where the bias arose because the average volume equivalent coating thickness was dominated by the thickly coated smaller particles present in large numbers, whereas most of light absorption was due a small number of thinly coated larger particles (Fierce et al., 2016, 2020). The magnitude of this bias depends on the fraction of multiply charged particles in the size-classified aerosol. Fig. S5a,d shows that 240 nm soot and agglomerated CB aerosols contain a small fraction of multiply charged particles, while in 150 nm nigrosin and compact CB this fraction is significant (Fig. S5b,c). The fraction of multiply charged particles is low for soot and agglomerated CB because the 240 nm particle mode is on the far right slope of the size distribution (Fig. S1) where the number of larger particles that could acquire multiple charges is low. As shown in the previous section for bare particles, by working with particle sizes on the right slope of the distribution, the impact of multiple charging can be greatly reduced without any additional measures. Alternatively, the measured data must be corrected to account for the significantly different growth rates of singly and multiply charged particles, *e.g.*, by following the approach described in SI, where a simple expression is derived based on continuum-regime condensation law for coating thickness difference between two spherical particles of different diameters (Text S6). As illustrated by dashed lines in Figs. 7 and 8, accounting for the slower growth rate of multiply charged particles generally improves the agreement with the measured absorption and scattering enhancements. However, calculated SSA remains significantly underestimated relative to measurements even after correction.

Notably, in the case of fractal soot, applying multiple charge correction produces inconsistent outcomes between different optical parameters. Absorption enhancement is improved only marginally whereas scattering enhancement becomes worse. The agreement is especially poor for thickly-coated aggregates that have collapsed into near-spheres. For example, for coated soot at the highest measured volume equivalent coating thickness, charge-corrected Mie underestimates the scattering enhancement by 40% and overestimates the absorption enhancement by 6%. This is counterintuitive because fully compacted core–shell morphologies should be well reproduced by Mie theory, i.e., the agreement for thickly coated soot should be better than the agreement for thinly

coated soot. However, it is possible that even after restructuring the real geometry of such compact coated aggregates deviates from the center-symmetric core–shell model implicit of Mie. Another explanation is that we are comparing enhancements relative to optical cross sections of bare particles, where the baseline bare particle cross sections are poorly predicted by Mie due to fractal morphology of bare soot. As shown by previous theoretical studies (Kahnert & Kanngießer, 2020; Zhang, Mao, Yin, & Wang, 2017), absorption enhancements are lower when the absorbing core (sphere or aggregate) is located away from the center and closer to the periphery.

3.2.6. Explicit treatment of fractal soot particles in optical calculations

To verify if the remaining disagreement between experimental and predicted optical properties of soot can be eliminated using a more explicit representation of fractal particle morphology, we performed DDA calculations on bare and coated soot aggregates. Numerical soot aggregates with fractal dimensions (D_f) ranging from 1.8 (fractal) to 2.7 (nearly compact) were considered. The pre-factor (k_0) was 1.3 for all aggregates. These aggregates consisted of 120 primary spheres, 28 nm in diameter each. Their mass corresponded to the mass of 245.3 nm mobility diameter particles for fractal soot or 190.3 nm for compact CB, based on our mass-mobility measurements. A uniform coating model was chosen because such morphological mixing state is expected in the case of DOS based on previous work (Chen et al., 2018). Details of the aggregate generation, discretization, and coating are described in Enekwizu et al. (2020). To calculate enhancements, cross sections of coated particles were normalized by cross section of bare fractal particles with $D_f = 1.8$.

Like with Mie calculations, DDA underestimates the absolute absorption and scattering cross sections of bare and coated particles by a large margin, as shown in Fig. 10c,d. Relative enhancements also deviate from the experiment (Fig. 10a,b), but generally to a lesser extent. For absorption, the difference in enhancements between aggregates of different D_f is less significant, confirming that absorption is mostly affected by increasing coating volume and not restructuring. Scattering enhancements predicted by DDA for coated fractal aggregates with $D_f = 1.8$ agree well with experimental results at low volume equivalent coating thicknesses, but start diverging at volume equivalent coating thicknesses above 20 nm (Fig. 10). The scattering enhancement is overestimated most significantly for the aggregates of a higher D_f.

Although DDA can be used to calculate the optical properties of an aggregate of complex geometry, its prediction accuracy is dependent on how realistically the aggregate is represented. Electron microscopy images show the existence of a large number of morphological features in soot samples, such as polydispersity in primary particle size, non-spherical primary particles, and overlapping and necking between neighboring primary particles (Chakrabarty, Garro, Chancellor, Herald, & Moosmüller, 2009; Yon et al., 2015). To obtain closure with the experiment, these features must be included in the aggregate models used in DDA calculations, as they have an impact on the optical properties of soot (Teng, Liu, Schnaiter, Chakrabarty, & Liu, 2019). Among these features, necking is most significant, as it enhances the electromagnetic coupling between interacting primary particles, resulting in stronger absorption and scattering. Thus, the assumption of point-touch contacts between spherical primary particles of a constant diameter in our DDA simulations is likely to introduce discrepancy in the calculated optical properties of soot. For instance, in experiments we observe a slight decline in absorption enhancement at a volume equivalent coating thickness of around 20 nm, a trend not accounted for by DDA. We speculate that this trend in experimental data is due to breaking of necks in the aggregate. It is at 20 nm volume equivalent coating thickness that maximum compaction is reached, corresponding to the maximum number of necks in the aggregate becoming fractured.

To separate the contributions from restructuring and coating addition to light scattering, we compared scattering enhancements between coated-denuded experiments and DDA calculations on bare aggregates of different D_f (1.8 to 2.7), as shown in Fig. 11. To overlay experimental scattering enhancements, which are a function of volume equivalent coating thickness, and modeled scattering enhancements, which are a function of D_f, coating thickness of 0 nm was set to be equivalent to $D_f = 1.8$. Since we know from coated-denuded GF_d measurements that particles reach maximum compaction, we assumed that the highest volume equivalent coating thickness corresponds to D_f of 2.7. An exponential decay function was used to map volume equivalent coating thicknesses to fractal dimensions between these two points, as described in supplemental information (Section S5). DDA calculations performed for 40-primary sphere aggregates, which correspond to 154 nm mobility diameter fractal particles, show an agreement with the experiment, pointing to the addition of coating as the major source of the discrepancy between experimental and DDA predicted scattering enhancements in coated soot aggregates. Choosing a more complex coating distribution model might have improved the agreement (Luo et al., 2019), but mapping the actual coating distribution from microscopy images was not possible in the present study because relatively volatile DOS rapidly evaporated under high vacuum in the SEM instrument.

4. Conclusion

We explored the impact of condensational processing on optical properties of soot and its surrogates — carbon black and nigrosin. The effects of coating addition were decoupled from the effects of morphological changes and experimental results were compared between surrogates and commonly used optical models. For fractal soot, the change in optical properties upon coating is driven by two processes: increasing particle volume due to coating addition and restructuring of the fractal core by the liquid coating. Increasing volume produces the largest contribution, resulting in an increase in both scattering and absorption. Restructuring affects only light scattering and its maximum contribution to enhancement is about 50%, which is reached when maximum compactness is achieved, beyond which a particle cannot restructure further. Absorption is only enhanced due to coating addition by the growing coating layer and not by restructuring, similar as shown by Forestieri et al. (2018).

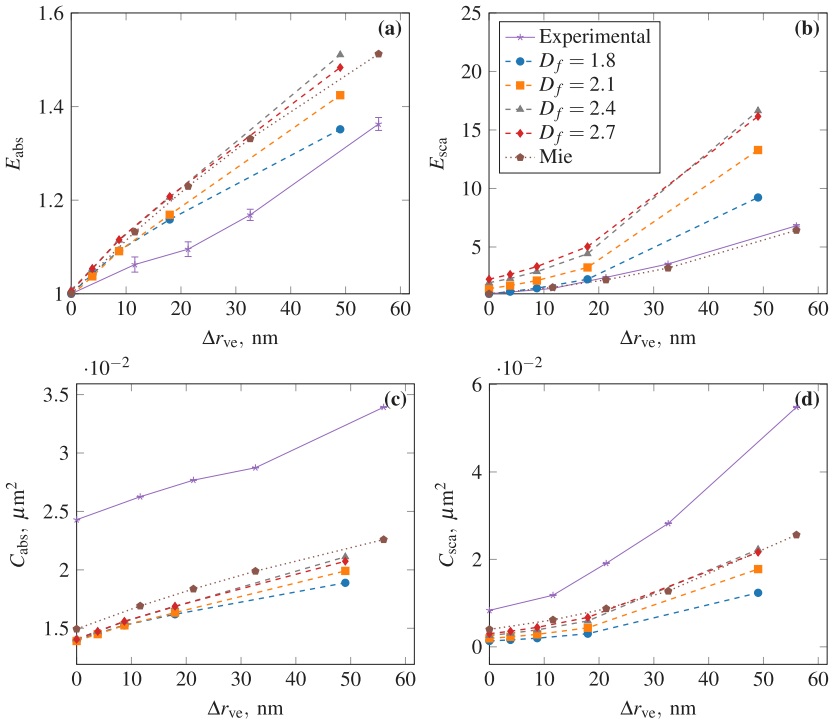

Fig. 10. Comparison of DDA calculations for aggregates of different compactness coated by DOS against experimental measurements and Mie calculations for coated volume equivalent spheres: (a) absorption and (b) scattering enhancements; (c) absorption and (d) absolute cross sections.

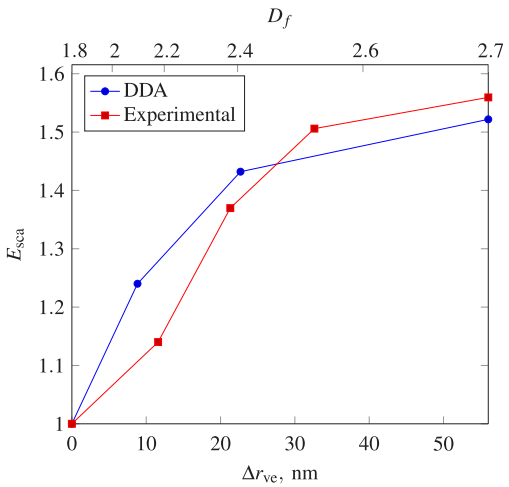

Fig. 11. Experimental scattering enhancements for coated-denuded aggregates *versus* volume equivalent coating thickness and DDA-calculated scattering enhancements *versus* fractal dimension.

We found that carbon black aggregates produced by nebulization of aqueous suspensions are similar in morphology to nearly-fully or fully restructured soot. Studies concerned with restructuring of soot aggregates should not use carbon black as a surrogate because some of the effects will not be reproduced correctly. However, in studies where the effects of restructuring do not need to be considered, such as when coating thicknesses are so high that a soot aggregate is collapsed, CB is a reasonable surrogate for soot. As to nigrosin, it can be used as a model for light-absorbing aerosols in general, but is not representative of optical properties of soot. Not only do nigrosin particles have a different morphology, but they also have a different complex refractive index than soot. Nevertheless, nigrosin particles are spherical and can be used with Mie theory for instrumental calibration.

The difference in complex refractive indices between soot and its surrogates can contribute to different optical responses during particle processing. Being the same material chemically, CB and mature soot are expected to have similar refractive indices. However,

variability in the degree of graphitization and the number of void fractions can cause the refractive index of soot to vary (Kahnert & Kanngießer, 2020), introducing additional uncertainties when comparing with models and between different research groups. For nigrosin, the imaginary part of the complex refractive index is significantly lower than that of soot. Hence, although for spherical 150 nm particles coated by DOS predicted enhancement in light absorption is similar between soot and nigrosin (within 4% for the 40 nm coating thickness), predicted enhancement in light scattering and SSA are significantly different, by 25% and 32%, respectively. Thus, using nigrosin as a surrogate of soot may lead to a significant underestimation of light scattering by coated combustion aerosols.

In agreement with previously reported experimental results (Forestieri et al., 2018; Khalizov et al., 2009), we show that the presence of multiply charged particles can significantly bias high measured optical cross-sections. Absolute optical cross sections are biased high because larger particles scatter and absorb more light. At the same time, relative enhancements are biased low because larger multiply charged particles acquire a lower coating thickness than smaller singly charged particles. When the fraction of multiply charged particles is significant, their presence needs to be accounted for. Alternatively, aerosol should be size-classified in such a way that there are only few particles that could attain multiple charges and have the same mobility as the primary size present in the generated aerosol. This usually means that the selected size lies far on the right slope of the size distribution.

When multiple charging is negligible or accounted for, Mie theory produces a reasonable agreement with experimental scattering enhancements, and to a lesser extent, with absorption enhancements, in some cases even outperforming DDA for fractal soot. Although Mie theory cannot account for the effect of compaction, the contribution of compaction to scattering enhancement is much lower than the effect of increasing volume for thickly coated particles. Hence, core–shell Mie agrees with experimental results for coated soot particles reasonably well and for many modeling applications it should provide a good enough estimate of optical enhancements. RDG agrees with absorption enhancements only for soot at low coating thicknesses, and is applicable for modeling absorption by lacey, non-restructured aggregates while they remain thinly coated. For bare soot aggregates, DDA predicts a compaction-driven increase in scattering in good agreement with our experimental results for coated-denuded soot, but it fares worse for coated aggregates. Since DDA is a rigorous model that calculates optical cross sections for arbitrary shapes, small morphological details of generated aggregates will have an effect on final results. Parameters such as fractal dimension, monomer diameter, necking, and coating distribution all need to be known to model soot aggregates accurately. The choice of these parameters may cause calculations to deviate from experiments. On the other hand, Mie acts as a “lumped-parameter” model for complex soot aggregates. It cannot capture minor variations in optics caused by varying morphology, but provides a good estimate for major effects caused by increasing coating volume. Another possible reason for its adequate performance is that the material refractive index of soot typically is inverted from experimental data using Mie theory (Chang & Charalampopoulos, 1990). In that case, the refractive index would be biased to minimize the difference between experimental data and optical properties predicted with Mie. That would also explain the discrepancy between experimental data and DDA calculations, as for DDA we need the true material refractive index and not some effective model-dependent value.

CRediT authorship contribution statement

Egor V. Demidov: Writing – review & editing, Writing – original draft, Visualization, Validation, Methodology, Investigation, Formal analysis, Conceptualization. **Ogochukwu Y. Enekwizu:** Writing – review & editing, Validation, Methodology, Investigation. **Ali Hasani:** Visualization, Investigation. **Chong Qiu:** Writing – review & editing, Methodology, Investigation, Formal analysis, Conceptualization. **Alexei F. Khalizov:** Writing – review & editing, Writing – original draft, Supervision, Resources, Project administration, Methodology, Investigation, Funding acquisition, Formal analysis, Conceptualization.

Declaration of competing interest

The authors declare that they have no known competing financial interests or personal relationships that could have appeared to influence the work reported in this paper.

Data availability

Data will be made available on request.

Acknowledgments

A.K. acknowledges the U.S. National Science Foundation, grants AGS-1554777 and AGS-2222104. C.Q. acknowledges the U.S. National Science Foundation Award AGS-1847019 and Buckman Endowed Fund at University of New Haven. E.D. is grateful for the NJIT Provost URI Summer Research Fellowship. We acknowledge the use of the SEM instrument at the Otto York Center for Environmental Engineering and Science at NJIT. We thank Ella Ivanova for creating a drawing for graphical abstract.

Appendix A. Supplementary data

Supplementary material related to this article can be found online at https://doi.org/10.1016/j.jaerosci.2024.106392.

References

Bluvshtein, N., Flores, J., Riziq, A. A., & Rudich, Y. (2012). An approach for faster retrieval of aerosols' complex refractive index using cavity ring-down spectroscopy. *Aerosol Science and Technology*, *46*(10), 1140–1150.

Bohren, C. F., & Huffman, D. R. (1983). *Absorption and scattering of light by small particles*. New York: Wiley.

Bond, T. C., & Bergstrom, R. W. (2006). Light absorption by carbonaceous particles: An investigative review. *Aerosol Science and Technology*, *40*(1), 27–67. http://dx.doi.org/10.1080/02786820500421521.

Brem, B. T., Mena Gonzalez, F. C., Meyers, S. R., Bond, T. C., & Rood, M. J. (2012). Laboratory-measured optical properties of inorganic and organic aerosols at relative humidities up to 95%. *Aerosol Science and Technology*, *46*(2), 178–190. http://dx.doi.org/10.1080/02786826.2011.617794.

Bueno, P. A., Havey, D. K., Mulholland, G. W., Hodges, J. T., Gillis, K. A., Dickerson, R. R., et al. (2011). Photoacoustic measurements of amplification of the absorption cross section for coated soot aerosol. *Aerosol Science and Technology*, *45*(10), 1217–1230.

Cappa, C. D., Onasch, T. B., Massoli, P., Worsnop, D. R., Bates, T. S., Cross, E. S., et al. (2012). Radiative absorption enhancements due to the mixing state of atmospheric black carbon. *Science*, *337*(6098), 1078–1081.

Chakrabarty, R. K., Garro, M. A., Chancellor, S., Herald, C., & Moosmüller, H. (2009). FracMAP: A user-interactive package for performing simulation and orientation-specific morphology analysis of fractal-like solid nano-agglomerates. *Computer Physics Communications*, *180*(8), 1376–1381. http://dx.doi.org/10.1016/j.cpc.2009.01.026.

Chang, H.-C., & Charalampopoulos, T. T. (1990). Determination of the wavelength dependence of refractive indices of flame soot. *Proceedings of the Royal Society of London. Series A: Mathematical and Physical Sciences*, *430*(1880), 577–591. http://dx.doi.org/10.1098/rspa.1990.0107.

Chen, C., Enekwizu, O. Y., Fan, X., Dobrzanski, C. D., Ivanova, E. V., Ma, Y., et al. (2018). Single parameter for predicting the morphology of atmospheric black carbon. *Environmental Science and Technology*, *52*(24), 14169–14179. http://dx.doi.org/10.1021/acs.est.8b04201.

Chen, C., Enekwizu, O. Y., Ma, X., Jiang, Y., Khalizov, A. F., Zheng, J., et al. (2020). Effect of organic coatings derived from the OH-initiated oxidation of amines on soot morphology and cloud activation. *Atmospheric Research*, *239*, Article 104905. http://dx.doi.org/10.1016/j.atmosres.2020.104905.

Chen, C., Enekwizu, O. Y., Ma, Y., Zakharov, D., & Khalizov, A. F. (2017). The impact of sampling medium and environment on particle morphology. *Atmosphere*, *8*(9), 162. http://dx.doi.org/10.3390/atmos8090162.

Chen, C., Fan, X., Shaltout, T., Qiu, C., Ma, Y., Goldman, A., et al. (2016). An unexpected restructuring of combustion soot aggregates by subnanometer coatings of polycyclic aromatic hydrocarbons. *Geophysical Research Letters*, *43*(20), 11,080–11,088. http://dx.doi.org/10.1002/2016GL070877.

China, S., Scarnato, B., Owen, R. C., Zhang, B., Ampadu, M. T., Kumar, S., et al. (2015). Morphology and mixing state of aged soot particles at a remote marine free troposphere site: Implications for optical properties. *Geophysical Research Letters*, *42*(4), 1243–1250. http://dx.doi.org/10.1002/2014GL062404.

Chylek, P., & Wong, J. (1995). Effect of absorbing aerosols on global radiation budget. *Geophysical Research Letters*, *22*(8), 929–931.

Coderre, A. R., Thomson, K. A., Snelling, D. R., & Johnson, M. R. (2011). Spectrally resolved light absorption properties of cooled soot from a methane flame. *Applied Physics B*, *104*(1), 175–188. http://dx.doi.org/10.1007/s00340-011-4448-9.

Cross, E. S., Onasch, T. B., Ahern, A., Wrobel, W., Slowik, J. G., Olfert, J., et al. (2010). Soot particle studies—Instrument inter-comparison—Project overview. *Aerosol Science and Technology*, *44*(8), 592–611. http://dx.doi.org/10.1080/02786826.2010.482113.

Dial, K. D., Hiemstra, S., & Thompson, J. E. (2010). Simultaneous measurement of optical scattering and extinction on dispersed aerosol samples. *Analytical Chemistry*, *82*(19), 7885–7896. http://dx.doi.org/10.1021/ac100617j.

Dinar, E., Riziq, A. A., Spindler, C., Erlick, C., Kiss, G., & Rudich, Y. (2008). The complex refractive index of atmospheric and model humic-like substances (HULIS) retrieved by a cavity ring down aerosol spectrometer (CRD-AS). *Faraday Discussions*, *137*, 279–295.

Dixkens, J., & Fissan, H. (1999). Development of an electrostatic precipitator for off-line particle analysis. *Aerosol Science and Technology*, *30*(5), 438–453. http://dx.doi.org/10.1080/027868299304480.

Dong, J., Zhao, J. M., & Liu, L. H. (2015). Morphological effects on the radiative properties of soot aerosols in different internally mixing states with sulfate. *Journal of Quantitative Spectroscopy and Radiative Transfer*, *165*, 43–55. http://dx.doi.org/10.1016/j.jqsrt.2015.06.025.

Draine, B. T., & Flatau, P. J. (1994). Discrete-dipole approximation for scattering calculations. *Journal of the Optical Society of America A*, *11*(4), 1491–1499. http://dx.doi.org/10.1364/JOSAA.11.001491.

Drinovec, L., Jagodič, U., Pirker, L., Škarabot, M., Kurtjak, M., Vidović, K., et al. (2022). A dual-wavelength photothermal aerosol absorption monitor: design, calibration and performance. *Atmospheric Measurement Techniques*, *15*(12), 3805–3825.

Enekwizu, O., Singh, D., & Khalizov, A. (2020). Absorption and scattering of light by soot aggregates with uniform and pendular ring coatings. *Journal of Aerosol Science*, *147*, Article 105583. http://dx.doi.org/10.1016/j.jaerosci.2020.105583.

Fan, X., Dawson, J., Chen, M., Qiu, C., & Khalizov, A. (2018). Thermal stability of particle-phase monoethanolamine salts. *Environmental Science and Technology*, *52*(4), 2409–2417. http://dx.doi.org/10.1021/acs.est.7b06367.

Fierce, L., Bond, T. C., Bauer, S. E., Mena, F., & Riemer, N. (2016). Black carbon absorption at the global scale is affected by particle-scale diversity in composition. *Nature Communications*, *7*(1), 12361.

Fierce, L., Onasch, T. B., Cappa, C. D., Mazzoleni, C., China, S., Bhandari, J., et al. (2020). Radiative absorption enhancements by black carbon controlled by particle-to-particle heterogeneity in composition. *Proceedings of the National Academy of Sciences*, *117*(10), 5196–5203. http://dx.doi.org/10.1073/pnas.1919723117.

Filippov, A. V., Zurita, M., & Rosner, D. E. (2000). Fractal-like aggregates: Relation between morphology and physical properties. *Journal of Colloid and Interface Science*, *229*(1), 261–273. http://dx.doi.org/10.1006/jcis.2000.7027.

Flores, J. M., Washenfelder, R., Adler, G., Lee, H., Segev, L., Laskin, J., et al. (2014). Complex refractive indices in the near-ultraviolet spectral region of biogenic secondary organic aerosol aged with ammonia. *Physical Chemistry Chemical Physics*, *16*(22), 10629–10642.

Forestieri, S. D., Helgestad, T. M., Lambe, A. T., Renbaum-Wolff, L., Lack, D. A., Massoli, P., et al. (2018). Measurement and modeling of the multiwavelength optical properties of uncoated flame-generated soot. *Atmospheric Chemistry and Physics*, *18*(16), 12141–12159. http://dx.doi.org/10.5194/acp-18-12141-2018.

Haynes, W. M. (2014). *CRC handbook of chemistry and physics* (95th ed.). Hoboken, NJ: CRC Press.

Haywood, J., & Boucher, O. (2000). Estimates of the direct and indirect radiative forcing due to tropospheric aerosols: A review. *Reviews of Geophysics*, *38*(4), 513–543. http://dx.doi.org/10.1029/1999RG000078.

Ivanova, E. V., Emelianova, A., Khalizov, A. F., & Gor, G. Y. (2022). Molecular simulation of benzene adsorption in graphitic and amorphous carbon slit pores. *Journal of Chemical & Engineering Data*, *67*(7), 1765–1778.

Ivanova, E., Khalizov, A., & Gor, G. (2020). Kinetic model for competitive condensation of vapor between concave and convex surfaces in a soot aggregate. *Aerosol Science and Technology*, *55*(3), 302–315.

Jullien, R. (1987). Aggregation phenomena and fractal aggregates. *Contemporary Physics*, *28*(5), 477–493.

Kahnert, M., & Kanngießer, F. (2020). Modelling optical properties of atmospheric black carbon aerosols. *Journal of Quantitative Spectroscopy and Radiative Transfer*, *244*, Article 106849. http://dx.doi.org/10.1016/j.jqsrt.2020.106849.

Kahnert, M., Nousiainen, T., & Lindqvist, H. (2013). Models for integrated and differential scattering optical properties of encapsulated light absorbing carbon aggregates. *Optics Express*, *21*(7), 7974–7993. http://dx.doi.org/10.1364/OE.21.007974.

Kahnert, M., Nousiainen, T., Lindqvist, H., & Ebert, M. (2012). Optical properties of light absorbing carbon aggregates mixed with sulfate: assessment of different model geometries for climate forcing calculations. *Optics Express*, *20*(9), 10042–10058. http://dx.doi.org/10.1364/OE.20.010042.

Kerker, M., & Loebl, E. M. (1969). *The scattering of light and other electromagnetic radiation*. Academic Press.

Khalizov, A. F., Lin, Y., Qiu, C., Guo, S., Collins, D., & Zhang, R. (2013). Role of OH-initiated oxidation of isoprene in aging of combustion soot. *Environmental Science and Technology*, *47*(5), 2254–2263. http://dx.doi.org/10.1021/es3045339.

Khalizov, A. F., Xue, H., Wang, L., Zheng, J., & Zhang, R. (2009). Enhanced light absorption and scattering by carbon soot aerosol internally mixed with sulfuric acid. *The Journal of Physical Chemistry A*, *113*(6), 1066–1074. http://dx.doi.org/10.1021/jp807531n.

Kondo, Y., Sahu, L., Kuwata, M., Miyazaki, Y., Takegawa, N., Moteki, N., et al. (2009). Stabilization of the mass absorption cross section of black carbon for filter-based absorption photometry by the use of a heated inlet. *Aerosol Science and Technology*, *43*(8), 741–756. http://dx.doi.org/10.1080/02786820902889879, OA status: bronze.

Lack, D. A., Lovejoy, E. R., Baynard, T., Pettersson, A., & Ravishankara, A. (2006). Aerosol absorption measurement using photoacoustic spectroscopy: Sensitivity, calibration, and uncertainty developments. *Aerosol Science and Technology*, *40*(9), 697–708.

Lang-Yona, N., Rudich, Y., Segre, E., Dinar, E., & Abo-Riziq, A. (2009). Complex refractive indices of aerosols retrieved by continuous wave-cavity ring down aerosol spectrometer. *Analytical Chemistry*, *81*(5), 1762–1769. http://dx.doi.org/10.1021/ac8017789.

Liu, C., Teng, S., Zhu, Y., Yurkin, M. A., & Yung, Y. L. (2018). Performance of the discrete dipole approximation for optical properties of black carbon aggregates. *Journal of Quantitative Spectroscopy and Radiative Transfer*, *221*, 98–109. http://dx.doi.org/10.1016/j.jqsrt.2018.09.030.

Liu, L., Wang, H., Yu, B., Xu, Y., & Shen, J. (2007). Improved algorithm of light scattering by a coated sphere. *China Particuology*, *5*(3), 230–236. http://dx.doi.org/10.1016/j.cpart.2007.03.003.

Lohmann, U., & Feichter, J. (2005). Global indirect aerosol effects: a review. *Atmospheric Chemistry and Physics*, *5*(3), 715–737.

Long, C. M., Nascarella, M. A., & Valberg, P. A. (2013). Carbon black vs. black carbon and other airborne materials containing elemental carbon: Physical and chemical distinctions. *Environmental Pollution*, *181*, 271–286. http://dx.doi.org/10.1016/j.envpol.2013.06.009.

Luo, J., Zhang, Q., Luo, J., Liu, J., Huo, Y., & Zhang, Y. (2019). Optical modeling of black carbon with different coating materials: The effect of coating configurations. *Journal of Geophysical Research: Atmospheres*, *124*(23), 13230–13253.

Ma, X., Zangmeister, C. D., Gigault, J., Mulholland, G. W., & Zachariah, M. R. (2013). Soot aggregate restructuring during water processing. *Journal of Aerosol Science*, *66*, 209–219. http://dx.doi.org/10.1016/j.jaerosci.2013.08.001.

Mackowski, D. W. (1995). Electrostatics analysis of radiative absorption by sphere clusters in the Rayleigh limit: application to soot particles. *Applied Optics*, *34*(18), 3535–3545. http://dx.doi.org/10.1364/AO.34.003535.

McMurry, P. H., Wang, X., Park, K., & Ehara, K. (2002). The relationship between mass and mobility for atmospheric particles: A new technique for measuring particle density. *Aerosol Science & Technology*, *36*(2), 227–238.

Mikhailov, E. F., Vlasenko, S. S., Podgorny, I. A., Ramanathan, V., & Corrigan, C. E. (2006). Optical properties of soot–water drop agglomerates: An experimental study. *Journal of Geophysical Research: Atmospheres*, *111*(D7), http://dx.doi.org/10.1029/2005JD006389.

Moore, R. H., Ziemba, L. D., Dutcher, D., Beyersdorf, A. J., Chan, K., Crumeyrolle, S., et al. (2014). Mapping the operation of the miniature combustion aerosol standard (mini-CAST) soot generator. *Aerosol Science and Technology*, *48*(5), 467–479.

Moosmuller, H., Chakrabarty, R. K., & Arnott, W. P. (2009). Aerosol light absorption and its measurement: A review. *Journal of Quantitative Spectroscopy and Radiative Transfer*, *110*(11), 844–878. http://dx.doi.org/10.1016/j.jqsrt.2009.02.035.

Orsini, D., Wiedensohler, A., Stratmann, F., & Covert, D. (1999). A new volatility tandem differential mobility analyzer to measure the volatile sulfuric acid aerosol fraction. *Journal of Atmospheric and Oceanic Technology*, *16*(6), 760–772.

Pagels, J., Khalizov, A. F., McMurry, P. H., & Zhang, R. Y. (2009). Processing of soot by controlled sulphuric acid and water condensation—Mass and mobility relationship. *Aerosol Science and Technology*, *43*(7), 629–640.

Park, K., Kittelson, D. B., Zachariah, M. R., & McMurry, P. H. (2004). Measurement of inherent material density of nanoparticle agglomerates. *Journal of Nanoparticle Research*, *6*, 267–272.

Radney, J. G., You, R., Ma, X., Conny, J. M., Zachariah, M. R., Hodges, J. T., et al. (2014). Dependence of soot optical properties on particle morphology: measurements and model comparisons. *Environmental Science and Technology*, *48*(6), 3169–3176.

Ramanathan, V., & Carmichael, G. (2008). Global and regional climate changes due to black carbon. *Nature Geoscience*, *1*(4), 221–227.

Saathoff, H., Naumann, K.-H., Schnaiter, M., Schöck, W., Möhler, O., Schurath, U., et al. (2003). Coating of soot and (NH4) 2SO4 particles by ozonolysis products of α-pinene. *Journal of Aerosol Science*, *34*(10), 1297–1321.

Sedlacek, A., & Lee, J. (2007). Photothermal interferometric aerosol absorption spectrometry. *Aerosol Science and Technology*, *41*(12), 1089–1101. http://dx.doi.org/10.1080/02786820701697812, OA status: bronze.

Sedlacek, A. J., Lewis, E. R., Onasch, T. B., Lambe, A. T., & Davidovits, P. (2015). Investigation of refractory black carbon-containing particle morphologies using the single-particle soot photometer (SP2). *Aerosol Science and Technology*, *49*(10), 872–885. http://dx.doi.org/10.1080/02786826.2015.1074978.

Seinfeld, J. H., & Pandis, S. N. (2016). *Atmospheric chemistry and physics: from air pollution to climate change*. New York, UNITED STATES: John Wiley & Sons, Incorporated, Chapter 12.

Slowik, J. G., Cross, E. S., Han, J. H., Kolucki, J., Davidovits, P., Williams, L. R., et al. (2007). Measurements of morphology changes of fractal soot particles using coating and denuding experiments: Implications for optical absorption and atmospheric lifetime. *Aerosol Science and Technology*, *41*(8), 734–750.

Slowik, J. G., Stainken, K., Davidovits, P., Williams, L. R., Jayne, J. T., Kolb, C. E., et al. (2004). Particle morphology and density characterization by combined mobility and aerodynamic diameter measurements. Part 2: Application to combustion-generated soot aerosols as a function of fuel equivalence ratio. *Aerosol Science and Technology*, *38*(12), 1206–1222. http://dx.doi.org/10.1080/027868290903916.

Sorensen, C. M. (2001). Light scattering by fractal aggregates: A review. *Aerosol Science and Technology*, *35*(2), 648–687. http://dx.doi.org/10.1080/02786820117868.

Stipe, C. B., Higgins, B. S., Lucas, D., Koshland, C. P., & Sawyer, R. F. (2005). Inverted co-flow diffusion flame for producing soot. *Review of Scientific Instruments*, *76*(2), Article 023908. http://dx.doi.org/10.1063/1.1851492.

Tao, W.-K., Chen, J.-P., Li, Z., Wang, C., & Zhang, C. (2012). Impact of aerosols on convective clouds and precipitation. *Reviews of Geophysics*, *50*(2), RG2001.

Teng, S., Liu, C., Schnaiter, M., Chakrabarty, R. K., & Liu, F. (2019). Accounting for the effects of nonideal minor structures on the optical properties of black carbon aerosols. *Atmospheric Chemistry and Physics*, *19*(5), 2917–2931.

Veghte, D. P., Moore, J. E., Jensen, L., & Freedman, M. A. (2015). Influence of shape on the optical properties of hematite aerosol. *Journal of Geophysical Research: Atmospheres*, *120*(14), 7025–7039. http://dx.doi.org/10.1002/2015JD023160.

Wentzel, M., Gorzawski, H., Naumann, K. H., Saathoff, H., & Weinbruch, S. (2003). Transmission electron microscopical and aerosol dynamical characterization of soot aerosols. *Journal of Aerosol Science*, *34*(10), 1347–1370. http://dx.doi.org/10.1016/S0021-8502(03)00360-4.

Yon, J., Bescond, A., & Liu, F. (2015). On the radiative properties of soot aggregates part 1: Necking and overlapping. *Journal of Quantitative Spectroscopy and Radiative Transfer*, *162*, 197–206. http://dx.doi.org/10.1016/j.jqsrt.2015.03.027.

Yurkin, M. A., & Hoekstra, A. G. (2020). User manual for the discrete dipole approximation code ADDA 1.4.0.

Yurkin, M. A., & Kahnert, M. (2013). Light scattering by a cube: Accuracy limits of the discrete dipole approximation and the T-matrix method. *Journal of Quantitative Spectroscopy and Radiative Transfer*, *123*, 176–183. http://dx.doi.org/10.1016/j.jqsrt.2012.10.001.

Zangmeister, C. D., Grimes, C. D., Dickerson, R. R., & Radney, J. G. (2019). Characterization and demonstration of a black carbon aerosol mimic for instrument evaluation. *Aerosol Science and Technology*, *53*(11), 1322–1333. http://dx.doi.org/10.1080/02786826.2019.1660302.

Zangmeister, C. D., & Radney, J. G. (2018). *NIST interlaboratory study of aerosol absorption measurements using photoacoustic spectroscopy: Report NIST TN 1989*, National Institute of Standards and Technology.

Zangmeister, C. D., You, R., Lunny, E. M., Jacobson, A. E., Okumura, M., Zachariah, M. R., et al. (2018). Measured in-situ mass absorption spectra for nine forms of highly-absorbing carbonaceous aerosol. *Carbon*, *136*, 85–93. http://dx.doi.org/10.1016/j.carbon.2018.04.057.

Zhang, X., Mao, M., Yin, Y., & Wang, B. (2017). Absorption enhancement of aged black carbon aerosols affected by their microphysics: A numerical investigation. *Journal of Quantitative Spectroscopy and Radiative Transfer*, *202*, 90–97. http://dx.doi.org/10.1016/j.jqsrt.2017.07.025.